THESIS

SINGLE-BLIND CONTROLLED RELEASE TESTING TO EVALUATE THE PERFORMANCE OF AN IN-SITU METHANE DETECTION SYSTEM.

Submitted by
Semiu Temidayo Fasasi
Department of Mechanical Engineering

In partial fulfillment of the requirements
For the Degree of Master of Science
Colorado State University
Fort Collins, Colorado
Summer 2025

Master's Committee:

Advisor: Daniel B. Olsen
Co-Advisor: Daniel J. Zimmerle

Timothy L. Vaughn
Jeffrey L. Collet

ABSTRACT

SINGLE-BLIND CONTROLLED RELEASE TESTING TO EVALUATE THE PERFORMANCE OF AN IN-SITU METHANE DETECTION SYSTEM.

The accurate detection and quantification of Methane (CH_4) emissions from equipment at oil and gas facilities is critical for resolving environmental concerns associated with Greenhouse Gas (GHG). This study presents the evaluation of a proprietary CH_4 detection solution deployed at a simulated oil and gas wellhead configuration on a green field site in south Texas. In this study, an automated controlled release rig was developed and used to conduct a single-blind, controlled release test program using a protocol developed specifically for the solution under test. The test program lasted for 57 days and included 5,153 discrete 15-minute reporting intervals with release rates ranging from 0.5 kgh^{-1} to 37.5 kgh^{-1}, and release durations ranging from 15 minutes to 3 hours. Upon completion of testing, a binary classification scheme was used to evaluate the performance of the solution by comparing the reports from the solution to the ground-truth emissions generated by the controlled release rig. For controlled releases greater than 2.5 kgh^{-1}, the solution showed a true positive rate (TPR) of 86 %, and a false negative rate (FNR) of 14 %. For release rates less than 2.5 kgh^{-1} the solution showed true negative rate (TNR) of 99.8 %, and a false positive rate (FPR) of 0.2 %. The solution showed a 90 % probability of reporting emissions greater than 5.5 kgh^{-1} and a 50 % probability of reporting emissions greater than 4.4 kgh^{-1}. The solution performance improved with increasing wind speed with 90 % and 50 % probability of reporting decreasing to 3.8 kgh^{-1} and 3.0 kgh^{-1}, respectively, for wind speeds greater than 2 ms^{-1}.

ACKNOWLEDGEMENTS

First and foremost, I would like to express my deepest gratitude to my advisors, Dr. Timothy L. Vaughn, Dr. Daniel J. Zimmerle, and Dr. Daniel B. Olsen. Their knowledge and perception have greatly influenced this work and my development as a researcher.

I would like to express my gratitude to my committee member, Prof. Jeffrey L. Collett, for his insightful comments and contributions to this effort. His observations deepened my comprehension and substantially improved the caliber of my study.

Furthermore, I would like to express my sincere gratitude to Colorado State University's Methane Emissions Technology Evaluation Center for providing the infrastructure and resources required to carry out this study. I also acknowledge my colleagues and peers who offered their technical expertise and moral support during challenging times.

A special thank you to my family and friends, who have been a source of inspiration and motivation throughout my academic path with their everlasting support and belief in my skills. Their support helped me stay centered and grounded.

I also want to thank Colorado State University's Mechanical Engineering Department instructors and staff for their help and encouragement while I was here.

Finally, I dedicate this work to everyone who works to promote innovation and knowledge for a sustainable future. Thank you all for making this journey memorable and fulfilling.

DEDICATION

I dedicate this thesis to God for His unwavering grace; to my parents for their sacrifices and constant belief in me; to my siblings and loved ones for their encouragement and prayers; to everyone whose quiet support and presence helped me reach this milestone; and to all who work to promote innovation and knowledge for a sustainable future.

TABLE OF CONTENTS

LIST OF TABLES

LIST OF FIGURES

Chapter 1

Introduction

1.1 Background of the Study

CH_4, an organic compound and natural gas component is a potent greenhouse gas that has proven to have higher Global Warming Potential (GWP) than Carbon-dioxide (CO_2) over 20 years [1, 2], and leads to air pollution, harmful to man and the environment. The CH_4 molecule traps twenty-eight times more heat than the CO_2 molecule in the atmosphere over a hundred year period [3, 4]. The primary source of CH_4 emissions comes from human activities such as fossil fuel extraction and use, agriculture, and waste management [5–8]. According to U.S. Environmental Protection Agency (EPA) as shown in Figure 1.1, the largest contributor of CH_4 emissions in the United States (U.S.) is the Oil and Gas (O&G) industry. They account for 28 % of emissions due to fugitive leaks from infrastructure, intentional venting and flaring during production, resulting in environmental hazards. [9–12]. 25 % of the total agricultural CH_4 emissions in the U.S. come from enteric fermentation [13, 14], and 16 % from landfills in waste management, where the emission is produced from anaerobic digestion based on moisture content, waste quantity, and the degree of temperature [8, 14–16]. As such, the aim of CH_4 detection and quantification solutions (solutions) is to accurately detect, and quantify CH_4 emissions with the goal of mitigating GHG. The mitigation goals may be driven by regulatory standards, or by compliance and participation with other programs such as Intergovernmental Panel on Climate Change (IPCC) and Oil & Gas Methane Partnership (OGMP) aimed at reducing GHG. Due to confidentiality agreements with the manufacturer, the specific type and configuration of the technology used in this study cannot be disclosed. Therefore, the system is referred to as "solution" throughout this thesis.

Various solutions have been deployed, ranging from traditional survey methods to continuous monitoring solutions to measure the presence of CH_4 in the environment [17]. Traditional survey methods typically involve direct sampling and analysis using specialized approaches and instruments such as Method 21 or Optical Gas Imaging (OGI) to detect emissions [18]. According to Cusworth et al. (2021), traditional detection methods have been limited in detecting CH_4 emissions from O&G facilities accurately with the possibility of overlooking emissions from unlit flares, uncontrolled tanks, and gas pneumatics. [19–23]. It is challenging to use the traditional survey method in large-scale emission monitoring, due to its cost and labor intensiveness, especially when estimating emissions from thousands of pieces of O&G equipment [17, 24]. The CM solution mitigates these drawbacks using its ability to monitor for intermittent and continuous emissions over longer periods of time, continuously, to identify leaks [2, 22, 25–27] rather than individual site visits. A CM solution uses a combination of sensing technologies to continuously identify emissions. There are numerous CM solutions which can be broadly placed into categories of PSN, and scanning/imaging solutions. Both of these solution types are commonly used in the O&G industry [17, 18, 28]. In CM solution, several variables can have a substantial impact on the accuracy and dependability of detections and the efficacy of CM solution performance including sensor location, weather, and detection algorithms. Evaluation of solution performance has been the focus of testing protocols, including those created under initiatives such as the Advanced Development of Emissions Detection (ADED) project and the Advanced Research Projects Agency-Energy (ARPA-E) Methane Observation Networks with Innovative Technology to Obtain Reductions (MONITOR) program, to standardize performance assessment of CM solutions [29, 30]. Some solutions that have participated in one or more of the aforementioned studies have shown good performance and detection capabilities, with some attaining True Positive Rate (TPR) greater than 80 % across the wide variety of tests [2]. Despite this, solutions typically tend to under-report actual CH_4 emission rates of releases, and show drawbacks in their ability to perform accurately under varying environmental conditions (humidity, wind speed and wind direction) and deployment strategies (sensor placement, height and orientation), which are crucial factors for regulatory compliance [2,31].

To mitigate these limitations, previous studies have employed single-blind testing to objectively evaluate solution performance and provide evidence that the CH_4 detection solutions function dependably in real-world scenarios. In single-blind testing, CH_4 emissions are simulated in a controlled setting without the solution being aware of the precise release conditions beforehand. This approach reduces potential bias in the interpretation of the solution's performance and provides more accurate insight into the solution performance under a range of conditions [32]. Single-blind controlled release testing frequently uses controlled, standardized release gases with different emission rates and environmental conditions to mimic real-world scenarios. For example, Colorado State University (CSU), Methane Emission Technology Evaluation Center (METEC) uses single-blind controlled release test to investigate detection limits, quantification accuracy, and localization precision of different CH_4 solutions [17,18,33]. Single-blind controlled release testing can vary in complexity depending on the specific information withheld from the participant. During the ADED project at METEC the solutions participating in the performance evaluation were blind to the timing, emission rate, duration, and location of methane releases [17,18,33]. In contrast, for this study, the solution under evaluation is unaware of the timing, release rate, and duration of the releases, but is informed of the release location. This removes certain variables from the performance requirements, such as the need to localize the leak source. These tests involve varieties of emission rates representing the ranges of those expected to be encountered under operational conditions, and continuous testing long enough to accommodate variation in wind speed and direction that one would expect to experience in the field. [19,34,35]. Thus, the need to establish how accurate and reliable these solutions perform requires a rigorous performance evaluation method carried out in this study.

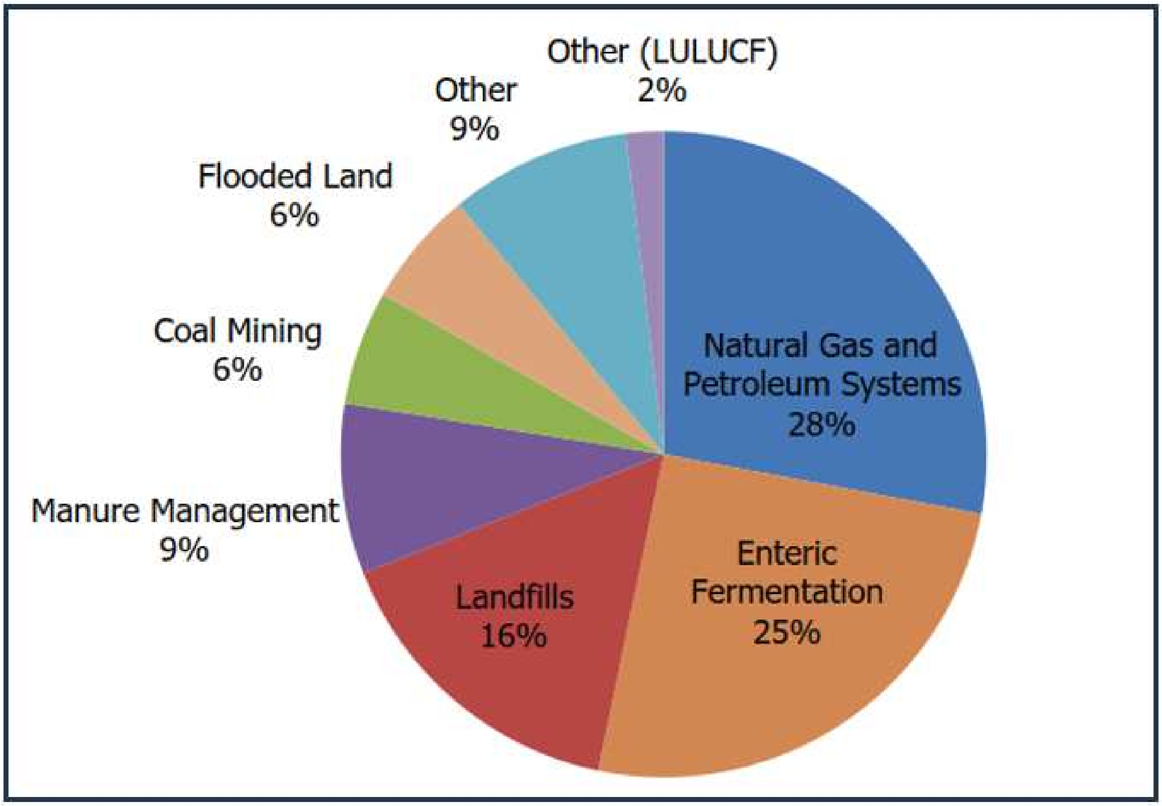

Figure 1.1: Methane emission sources in the United States.

1.2 Objectives of the Study

The primary aim and objective of this study is to evaluate the performance of a CH_4 detection solution through single-blind controlled release testing. The specific objectives include:

- To develop a hardware system (the controlled release rig) to test the capabilities of the CH_4 detection and measurement solution in actual operating facilities and other remote locations.

- Use the controlled release rig to perform independent, single-blind controlled release tests to assess the performance of the solution.
  - Design a test specific to a particular CH_4 monitoring solution.
  - Inform future design of a test protocol broadly applicable to a variety of CH_4 monitoring solutions

1.3 Scope of the Study

This thesis focuses on a single-blind controlled release test that was performed at a single site in South Texas shown in Figure A.1. The test activities include controlled releases of natural gas at varying flow rates and environmental conditions. In this study, a typical O&G wellhead configuration that mimics an actual operational facility was used in the evaluation of a particular CH_4 detection solution carried out from March 12 to May 8, 2024 (57 days). Although the results can be applied to comparable CH_4 detection solutions, they may not be generalized to all CH_4 monitoring solutions or environmental conditions.

Figure 1.2: Example of oil and gas wellhead.

1.4 Significance of the Study

In this study, we performed a single-blind controlled release testing at a site that mimics an actual O&G operational facility to assess the performance of an in-situ CH_4 detection solution. This research is important for several reasons, including the advancement of CH_4 detection solutions, contribution to health and safety, and support for policy and decision making. The study contributes to the development of reliable and accurate CH_4 monitoring solution through the evaluation of the solution's performance. This evaluation helps inform where and how the technology can be improved to better support GHG mitigation in O&G facilities. The study contributes to health and safety by enabling early detection of methane leaks, thereby supporting timely intervention or emergency response, protecting nearby communities from harmful gas migration, and avoiding potential hazards such as fires and explosions. The accurate detection of CH_4 emissions is crucial for policymaking. The findings from this study can serve as a reliable reference to inform regulatory decision-making, particularly in the context of compliance with EPA regulations such as 40 Code of Federal Regulations (CFR) Part 60, Subpart OOOO(b), including the performance standards outlined in Tables 1 and 2 for fugitive emissions monitoring at O&G facilities [36]. Thus, the findings serve as objective evidence for regulatory agencies to assess whether the technology meets required thresholds for methane detection programs. The results can support the design and enforcement of Leak Detection and Repair (LDAR) regulations by identifying scenarios where the system is effective or limited in O&G facilities which certainly can improve confidence on assessment criteria and regulatory frameworks to reduce CH_4 emissions and support global efforts to mitigate climate change.

Chapter 2

Literature Review

2.1 CH_4 Detection Solutions

CH_4 detection solutions use various methods to detect and quantify CH_4 emissions. Various solutions have been deployed to estimate emissions ranging from the traditional survey method to the continuous monitoring solution [17]. CM solutions address the shortcomings of traditional survey methods for detecting CH_4 emissions [17]. In O&G, the CM solutions can be classified into two different categories according to the measurement principles, deployment and detection capabilities. PSN and scanning/imaging solutions.

- **PSN Solutions**

  These may use stationary point sensors, but generally use multiples of them, to form a sensor network deployed to monitor CH_4 emissions at O&G facilities [28,37]. PSN may use various types of technologies and sensors including Tunable Diode Laser Absorption Spectroscopy (TDLAS), pyroelectric, calorimetric, Semiconducting Metal Oxide (SMO), and resonant sensors. Sensors are typically deployed together with meteorological instruments whose data are combined with sensor outputs in various processing algorithms to form PSN solutions for CM [2,18,28].

  - *Tunable Diode Laser Absorption Spectroscopy (TDLAS)*

    TDLAS is an optical measurement technique that measures gas concentrations such as CH_4, nitrous oxide (N_2O), and water vapor [38]. TDLAS has the capability to carry out real-time measurements with high sensitivity and the ability to detect low CH_4 concentrations [39]. For CH_4 detection, the tunable laser light is absorbed at wavelengths that correspond to the absorption lines of CH_4, particularly around $1.65\,\mu m$ [39–41]. The methane concentration level is then deduced from the loss of light intensity according to the Beer–Lambert law, which defines a direct relationship between gas concentration and light absorption. Recent advancements in TDLAS technology have significantly enhanced methane detection sensitivity across various infrared bands. Using a Distributed Feedback Quantum Cascade Lasers (DFB-QCL) at 1275.04 cm^{-1} (7.84 µm), a minimum detection limit (MDL) of 5.9 ppb was achieved within 1 second over a 57.6 m optical path. A Interband Cascade Laser (DFB-ICL) operating at 2968.4 cm^{-1} to 2968.85 cm^{-1} (approximately 3.37 µm) demonstrated a detection limit as low as 560 ppt with a 580 m path length and a 290 s acquisition time. In the near-infrared region, a Distributed Feedback Laser Diode (DFB-LD) system at 4297.56 cm^{-1} (approximately 2.33 µm) achieved a 36 ppb MDL using a 72 m path and a 137 s measurement duration. These examples highlight the capability of TDLAS to achieve sub-ppb methane detection when optimized with appropriate laser sources and absorption path configurations [42, 43]. However, the performance of TDLAS can be affected by noise and interference which could be caused by fluctuation of laser light, impurities in the environment, and optical interference [40, 44].

- *Pyroelectric Sensors*

  Pyroelectric sensors have the ability to identify variations in Infrared Radiation (IR) that make them suitable for PSN solutions. They are frequently used as gas analyzers, laser detectors, thermal analyzers, and fire alarms. Pyroelectric CH_4 sensors have several benefits, such as a broad measurement range, good sensitivity and responsiveness, and the capacity to function without oxygen [28, 37, 45]. Pyroelectric sensors have the ability to detect CH_4 as low as 5.6 ppm at a response time of 3 s [46]. However, for effective performance, pyroelectric sensors typically require a high power supply to generate and maintain constant heat, which limits their applicability in many practical settings including PSN solution deployment [37,47].

- *Calorimetric Sensors*

  The working mechanism of the calorimetric sensor is based on the principle that a chemical reaction (catalytic combustion) or a physisorption process (the process by which an atom or molecule in the gas phase adheres to a solid surface) absorbs or releases heat [48,49]. As such, the calorimetric sensor consists of a reference element and a catalyst-sensing element that detects CH_4 emissions by measuring the heat emitted during the oxidation of CH_4 [48,50]. Nevertheless, for this type of sensor, the limitation is that the catalyst is prone to poisoning when some gases (Phosphate, Carbon monoxide, Cyanides etc.) are present, and there is need for recalibration. Also, the enthalpy change during the catalytic combustion is significant because it directly influences the sensor's ability to detect CH_4. Thus, the calorimetric gas sensors may work poorly and detect CH_4 emissions incorrectly if there is a slight change in the enthalpy of combustion brought on by a change in the analyte concentration [51].

- *SMO* Sensors

  SMO sensors depend on oxidation-reduction (REDOX) reaction between SMO and the target gases for detection. SMO sensors are classified into two types: p-type, and n-type [37,52]. The primary carrier of p-type SMOs is the "hole". Holes are formed by doping semiconductors with group 3 elements from the periodic table which lack valence electrons. The n-type SMOs use electrons as their primary carrier and are naturally produced by oxygen vacancies and are suitable for developing CH_4 sensors [37]. SMO sensors may have low selectivity because they can easily respond to other organic compounds leading to False Positive (FP) detections. They may also exhibit poor recovery rates; it takes a much longer time for an SMO to return to baseline readings when analyte concentrations fall compared to optical sensors like TDLAS or Non-Dispersive Infrared (NDIR). At room temperature or temperatures below 150 °C, the response time is usually more than 5 minutes. Higher temperatures, up to 300 °C, are required to achieve response times of less than 1 minute [53]. SMOs are also impacted by humidity variations. Water molecules interact with the sensing materials and affect the surface reactions, leading to measurement errors [37,54,55].

- **Scanning/Imaging Solutions**

  Scanning/imaging solutions seek to build a spatial mapping of CH_4 concentrations using a variety of techniques. The mappings may be used only for detection, or may be used for quantification. For example, LIDAR systems build plume images by scanning a scene with laser pulses tuned to an absorption line of CH_4 gas and analyzing the reflected light signal to detect the concentration of CH_4 present along the path between the beam launch and the reflective surface. Imaging solutions (e.g., OGI) build plume images by mapping infrared radiation to a sensor array using a lens, much like a digital camera, except that it uses infrared-capable lenses and image sensors that convert infrared radiation to an image [17,18,56]. This provides a visual representation of CH_4 emissions, allowing operators to see CH_4 plumes in real-time.

  - *Optical Gas Sensor*

    An optical gas sensor is a type of gas sensor that uses light absorption, emission, or scattering to detect and measure the presence and concentration of specific gases. It identifies variations in electromagnetic waves or visible light resulting from an analyte's interaction with the receptor part (the receptor part is the component that specifically interacts with the target gas (analyte)) [37]. These sensors are widely used for environmental monitoring because they can offer high sensitivity, selectivity, and stability. IR absorption spectroscopy using mid-IR light is commonly used to identify the molecules quantitatively by analyzing the specific IR wavelengths that they absorb, which correlate with the distinct vibrational modes of their chemical interactions.

Based on this technique, CH_4 has a strong absorption line at 3.3 µm. The 3 µm to 3.7 µm wavelength range is significant because many gases that have carbon-hydrogen (C–H) bonds, like CH_4, all stretch in that region. The absorption at 3.3 µm is about 100 times stronger than at 1.65 µm, making it much easier to detect methane when using sensors that operate in that range [57, 58]. Optical gas sensors used in scanning/imaging solutions often exhibit greater sensitivity to heavier hydrocarbons such as ethane and propane, which can enhance plume visibility in mixed gas releases. However, their effectiveness in methane-specific detection is influenced more significantly by factors such as thermal contrast between the gas plume and its background, background thermal noise, and operator expertise. These factors often impose greater limitations than chemical sensitivity alone [59, 60].

- *Laser based Sensor*

  In scanning/imaging solutions, laser-based sensing technologies integrate high-resolution spectroscopy with spatial mapping methods to detect and visualize methane plumes in real time. These techniques include TDLAS and Differential Absorption LiDAR (DIAL), both of which exploit methane's unique absorption features in the near-IR (1.6 µm) and mid-IR (3.4 µm) spectral regions. In particular, TDLAS is widely deployed in field applications due to its high sensitivity and its compatibility with near-IR wavelengths, which allow for reduced cooling requirements and enhanced system efficiency [61]. For spatial mapping, systems such as Bridger Photonics' Gas Mapping LiDAR sweep laser beams across the target area using scanning optics or airborne platforms, capturing absorption across multiple lines of sight. This enables real-time or near-real-time visualization of methane plumes and leak localization over large areas [62, 63]. These solutions combine the advantages of spectroscopy and spatial coverage, allowing both qualitative visualization and quantitative concentration estimation. However, these systems have distinct trade-offs. Low-cost laser scanners, such as mechanical or Micro-Electro-Mechanical (MEMS)-based systems, often require several minutes to compile a complete plume image, limiting their use in real-time monitoring scenarios [64]. In contrast, fast-scanning or high-sensitivity systems capable of real-time imaging are often expensive and require complex optics and processing [65]. Furthermore, performance is highly dependent on target surface reflectivity (albedo) and atmospheric conditions, such as fog, dust, or rain, which can attenuate the laser signal [66, 67]. To maximize return signal and spatial coverage, scanners are often mounted on elevated platforms or drones, enabling wider field-of-view and better geometry for backscatter collection.

CM solutions may use any of the sensors described above, implemented together with meteorological data and algorithms to detect, measure, and estimate CH_4 emissions at O&G facilities. CM solutions may come to play an essential role in identifying sources and informing abatement decisions that help guide the reduction of CH_4 emissions at O&G facilities, furthering environmental protection and ensuring compliance with current and future GHG regulations. The classification of CM solutions into PSN, and scanning/imaging solutions demonstrates the variety of approaches available to mitigate CH_4 emissions, each with unique advantages and disadvantages for a given application.

2.2 PSN Solution Deployment

Solution deployment plays a critical role in the performance of PSN solutions. Effective sensor placement is a core component of a solution deployment for CH_4 detection.

Various techniques can be used, including sophisticated software packages. For example, Chama (a python package) [68], uses linear programming (mixed integer linear programming) to create monitoring plans, including placement of sensors to ensure sufficient coverage and maximize the sensitivity of the system [69, 70]. Sensors are typically placed in a spatially distributed network, often around the perimeter of a facility or in locations informed by prevailing wind patterns. Deployment considerations include sensor height and spacing, meteorological variability, and site layout constraints. The sensor height and spacing affects the solution's ability to intercept methane plumes. Meteorological variability, particularly wind speed and direction, influences plume transport and site layout constraints, which include obstructions like equipment or buildings [28, 70].

2.3 Analytics and Detection Algorithms

Analytics are central to turning raw sensor data into leak detections that can be acted upon. PSN solutions analyze the numerous incoming time series data streams using advanced algorithms to: distinguish between background and actual methane emissions; detect events using statistical thresholds, signal processing, or machine learning; and estimate emission source locations and rates, often by integrating dispersion models (e.g. Gaussian plume inversions) with observed data [69, 71]. Some studies have focused specifically on developing and improving advanced analytics and detection algorithms for CH_4 monitoring including machine learning techniques with geographical analysis, matched filter techniques, and online inverse Gaussian plume modeling. A critical factor influencing the performance of these analytics is the solution's Minimum Detection Limit (MDL). MDL is the lowest emission rate a solution can reliably detect. Understanding the interplay between dispersion behavior and MDL is essential for accurate emission detection, especially in complex atmospheric condition. [72]

Machine learning techniques and geographical analysis can enhance leak detection efficiency in CH_4 detection [71]. To detect leak-prone components and classify infrastructure by risk level, machine learning algorithms trained on historical leak data are implemented, and the Bayesian inference method can be used for quantifying emission rates to take uncertainty into account [71]. The study of Hongzhou et al. (2024) [73] uses the matched filter (a methane retrieval algorithm) to retrieve point source methane emission data above the background concentration, introducing an adaptive clustering algorithm to categorize cloud-free Sentinel-2 imagery over the computational area (Sentinel-2 is a multispectral, wide-swath, high-resolution imaging mission) [73]. The dispersion modeling is essential in understanding how gases such as methane behave after atmospheric releases. One commonly used dispersion model is the Gaussian plume model inverse. The Gaussian plume model inverse as shown in equation 2.1 estimates characteristics like source location or emission rate using wind speed, dispersion coefficient, methane concentration, and downwind distance to estimate and quantify methane emissions [74,75].

$$Q = C(x,y,z) \cdot 2\pi u \sigma_y \sigma_z \cdot \exp\left(\frac{y^2}{2\sigma_y^2}\right) \left[\exp\left(-\frac{(z-H)^2}{2\sigma_z^2}\right) + \exp\left(-\frac{(z+H)^2}{2\sigma_z^2}\right)\right]^{-1} \tag{2.1}$$

Where:

$C(x,y,z)$ Pollutant concentration at point (x,y,z) (mass per unit volume)

Q Emission rate of the pollutant (mass per unit time)

u Wind speed in the x-direction (m/s)

σ_y, σ_z Dispersion coefficients in the lateral (y) and vertical (z) directions, respectively (m)

H Effective stack height (actual stack height + plume rise) (m)

$\exp\left(-\frac{y^2}{2\sigma_y^2}\right)$ Gaussian distribution in the crosswind (y) direction

$\exp\left(-\frac{(z-H)^2}{2\sigma_z^2}\right) + \exp\left(-\frac{(z+H)^2}{2\sigma_z^2}\right)$ Reflection term accounting for dispersion above and below the ground

In the Gaussian plume model, the methane concentration decreases with increasing distance from the release point due to atmospheric dilution. Therefore, the plume may fall below a solution's MDL at a certain threshold distance, making detection unlikely beyond that range and thereby increasing the False Negative Rate (FNR) [72, 76]. This interaction between dispersion and MDL is critical. If dispersion is limited and the plume remains concentrated, even low-emission sources might be detected. Thus, the expected results from dispersion modeling not only inform sensor placement and test design but also help interpret sensor data in light of MDL limitations.

This study evaluates the performance of a PSN solution that employs TDLAS sensors to detect the presence or absence of CH_4 emissions at a simulated O&G facility in South Texas using single-blind controlled release testing. In PSN solutions, an array of sensors, deployment strategies, and analytics algorithms is combined to facilitate the conversion of methane concentration readings to interpretable detection information. The study contributes significantly to the efficient methane leak detection and mitigation efforts in the oil and gas industry.

Chapter 3

Materials and Methods

3.1 Experimental Design

To ensure an unbiased assessment of the sensitivity, accuracy, and dependability of the CH_4 detection solution, the CH_4 detection solution operator is unaware of the timing, duration, and release rates, but is aware of the location of the CH_4 release point. In this study, we developed an automated CRR that simulates O&G wellhead emission circumstances by releasing CH_4 at controlled flow rates according to a predefined test protocol. The test protocol includes random variation of CH_4 flow rates over a long test period to test the solution's detection capabilities across wide range of emission magnitudes, and provide an opportunity for testing under varying environmental conditions.

3.2 The Controlled Release Rig (CRR)

The CRR is a device designed to mimic CH_4 emissions at O&G facilities, but in a controlled manner. It is programmed to release known amounts of CH_4 from a designated point through a flexible tube to mimic potential emission sources at operational facilities. This enables the evaluation of the CH_4 detection solution under study by providing well-known, ground-truth emissions to compare to. Figure 3.1 shows the CRR developed and used to carry out the test. The device is fully automated with the following capabilities:

- Remote operation: start/stop gas flow, set gas flow rate, send output to 3 locations. All test functions can be monitored/operated remotely 24/7. The rig can be programmed to run autonomously.
- Flow rate range (0-50 kgh^{-1}) natural gas.

- Constant flow rates per single test (as defined by this protocol), or varying flowrates as desired.

- Weather station/sonic anemometer on telescoping mast.

Figure 3.1: The controlled release rig (Left side shows the conceptual CAD model, Right side shows the completed device in use during testing).

The device contains three compartments containing various components that make up the controlled release rig. The compartments include:

- The Flow Compartment

- The Communication System (COMMS) Compartment

- The Power Compartment

3.2.1 The Flow Compartment

The flow compartment contains the flow controller that controls for the mass flow rate of CH_4 releases delivered to the desired release point via flexible tubing attached to the outlet. In this study, three flow controllers were used: MCR-2000 for flow rates ranging from 0 to 1300 SLPM, MCR-250, for flow rates up to 250 SLPM, and MCR-50 for flow rates up to 50 SLPM.

3.2.2 The COMMS compartment

The main components in the COMMS compartment are the LabJack data acquisition switch, and the cellular modem/router that provides communications and remote control.

- *LabJack Data Acquisition Device*

  The LabJack gives the capability to read analog and digital signals from various sensors and switches. It has 23 channels of digital inputs and 10 channels of analogue inputs. The analog inputs are used to monitor the pressure sensors, while the digital inputs are used to monitor the state of the valves to inform the position of the CRR valves on the field or during operation and provide feedback for control signals. CB15 and CB37 expansion boards were attached to the LabJack T7 to provide sufficient digital input/output terminals.

- *Teltonika RUT955 Router*

  The router is used to facilitate connection between the data recording devices, and external monitoring systems. The RUT955 also facilitates remote access and monitoring, enabling real-time supervision of the experimental setup.

3.2.3 The Power Compartment

To ensure a reliable power supply for the CRR in remote or off-grid locations, a solar power system, a charge controller, and a battery were used for efficient power supply to the CRR.

Major Power System Design and Components

- *Solar panel*

  The solar panel, which converts sunlight into electrical energy, is the main source of power in this study. 200 W of 24 V solar panels were used to supply adequate power to the system.

- *Battery*

  A 24 V battery was used to store the power generated by the solar panels during the day for use during low sunlight weather conditions, like at night or during overcast weather. Absorbent Glass Mat (AGM) batteries were selected because of their moderate energy density, affordable cost, and reliable discharge performance at high and low temperatures outside the range of comparable lithium chemistry batteries.

- *Charge Controller*

  A 15 A Maximum Power Point Tracking (MPPT) solar charge controller was used to ensure adequate charging of the battery and optimal use of available solar irradiance to facilitate optimal performance of the CRR.

Power Compartment Sizing for the CRR Power Supply

To ensure that the CRR power system meets the desired needs, we estimate the sizing of each of the components: solar panel, battery, and charge controller by carrying out a power budget to avoid under-sizing or oversizing by accounting for the amount of power required by each component and keep the device running, store power, and function efficiently when there is a limited amount of sun to recharge the solar panel.

- *Solar Panel Sizing*

  For the selection of adequate solar panel capacity, the daily energy requirement to adequately power the CRR system was estimated. The system should produce enough energy to meet energy demands and recharge the battery storage. Assuming an average of 5 peak sun hours per day, the generated energy by the solar panel is estimated thus: For a 200 W solar panel:

$$E_{\text{solar}} = P_{\text{panel}} \times \text{Peak Sun Hours} \tag{3.1}$$

$$E_{\text{solar}} = 200W \times 5h = 1000Wh \tag{3.2}$$

  where E_{solar} is the energy generated by the solar panel, and P_{panel} is the solar panel power rating (load power).

- *Battery Sizing*

  Battery storage is selected to save excess solar power for use when there is no adequate sunlight hours. The system utilizes two 12 V, 42 Ah AGM batteries, configured in series to form a 24 V, 42 Ah bank. The total stored energy is:

$$E_{\text{battery}} = 24V \times 42Ah = 1008Wh \tag{3.3}$$

  E_{battery} is the total battery energy, and E_{usable} is the usable energy.

  Since AGM batteries should not be discharged beyond 50 % (depth of discharge) to maintain longevity [77], the usable energy is:

$$E_{\text{usable}} = 1008Wh \times 0.5 = 504Wh \tag{3.4}$$

Based on equation 3.4, we see that the 1000 Wh of energy generated is sufficient to recharge 504 Wh of the required usable battery energy, however real world conditions introduce some factors that result to loss of energy such as:

- *Battery charge efficiency* (85% for AGM batteries)
- *Solar charge controller efficiency* (90% for MPPT)
- *Temperature and shading losses*

Thus, the effective charging power $E_{\text{effective}}$, reaching the battery is:

$$E_{\text{effective}} = 1000Wh \times 0.85 \times 0.9 = 765Wh \tag{3.5}$$

This means that even with system inefficiencies which brings the effective energy to 765 Wh, a 200 W solar panel can sufficiently charge the battery bank to 504 Wh and still provide some margin of safety of about 261 Wh.

- *Charge Controller Selection*

  The system requires a charge controller suitable for estimated current accounted for a 200 W solar panel charging a 24 V battery.

  $I_{\text{controller}}$ is the charge controller current, V_{battery} is the battery voltage, and P_{solar} is the solar panel power rating.

$$I_{\text{controller}} = \frac{P_{\text{solar}}}{V_{\text{battery}}} \tag{3.6}$$

$$I_{\text{controller}} = \frac{200W}{24V} = 8.3A \tag{3.7}$$

To ensure efficient performance of the controller, a factor of safety between 1.25 and 1.5 was considered. Therefore:

$$I_{\text{controller}} = 8.3A \times 1.25 = 10.4A \tag{3.8}$$

$$I_{\text{controller}} = 8.3A \times 1.5 = 12.5A \tag{3.9}$$

Thus, a 15 A MPPT charge controller is suitable to ensure adequate performance of the CRR.

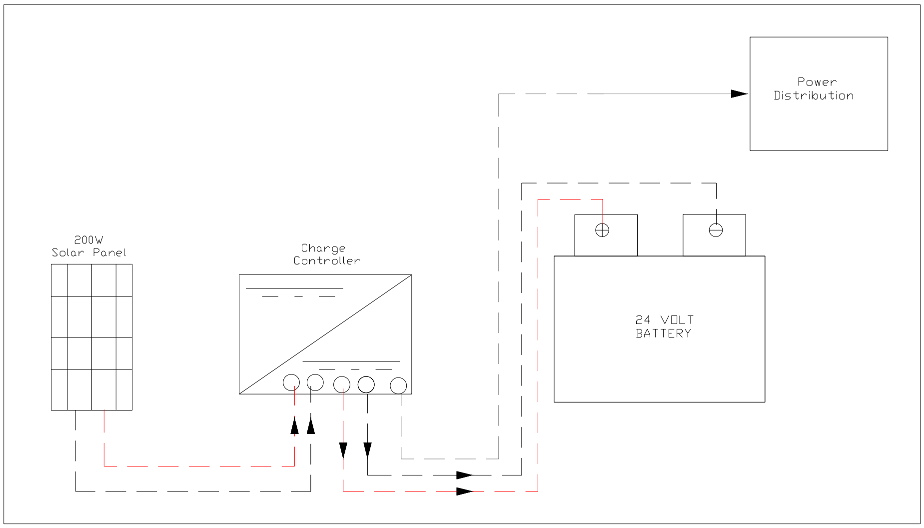

Figure 3.2: The Power Compartment, see Appendix G for the complete process and instrumentation diagram.

3.3 The Single-blind Test

The single-blind test in this study has three unknown parameters to the solution under test: start time, duration, and release rate. While the height and location of the natural gas release point were known, the flow rate, start time, and test duration duration were unknown to the solution, and were randomly generated. The testing included several "test periods" of both idle times when no controlled releases were performed and times when controlled releases were occurring, which were pre-programmed at a variety of emission rates. The test periods were generated randomly and uploaded to a custom web server that was developed for ethe xecution of the test.

Each test period lasted between 1 and 4 days. Emission rates were randomly selected to assess the performance of the solution for a wide range of release rates and wind conditions to create a Probability of Reporting (POR) curve that illustrates the performance of the solution for the entire testing program that lasted for 57 days. Each emission rate setpoint during the test period has one or more tests with 1-n reporting intervals by dividing the total duration per test into 15-minute reporting intervals matched with a constant controlled release emission rate. The 15-minute reporting interval is part of the specific protocol developed for the solution under test; the solution reports detections (or non-detections) at each 15-minute interval of the day, e.g., 00:00:00, 00:15:00, 00:30:00, 00:45:00, 01:00:00, etc. Each test period setpoint changes 3 minutes before reporting intervals and 1 minute after reporting intervals with random numbers of zero-emission periods between test periods. The randomly generated test period was created using a test program written in Python. This program executes various operations and generates key parameters for the single-blind test, including flow rate, timing, and duration. It also produces time-series plots that illustrate the expected detection performance of the solution under test based on the generated plan as shown in Figure 3.4. Furthermore, the program saves the test schedule as a Comma Separated Value (CSV) file, which is then uploaded to the web server shown in Figure B.1 where the execution of the single-blind controlled release test is controlled for the execution of the test.

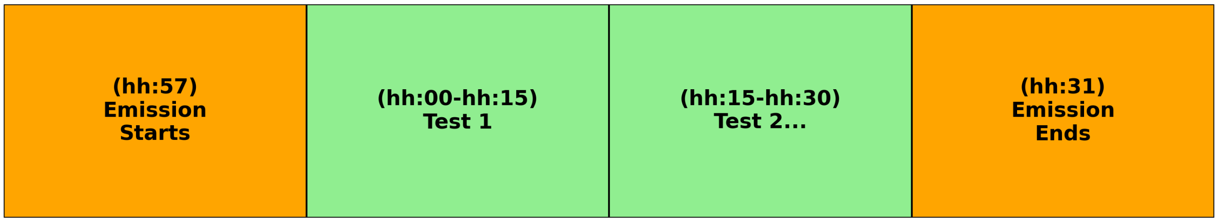

Figure 3.3: "Test" definition in relation to 15 minutes reporting intervals based on the defined protocol.

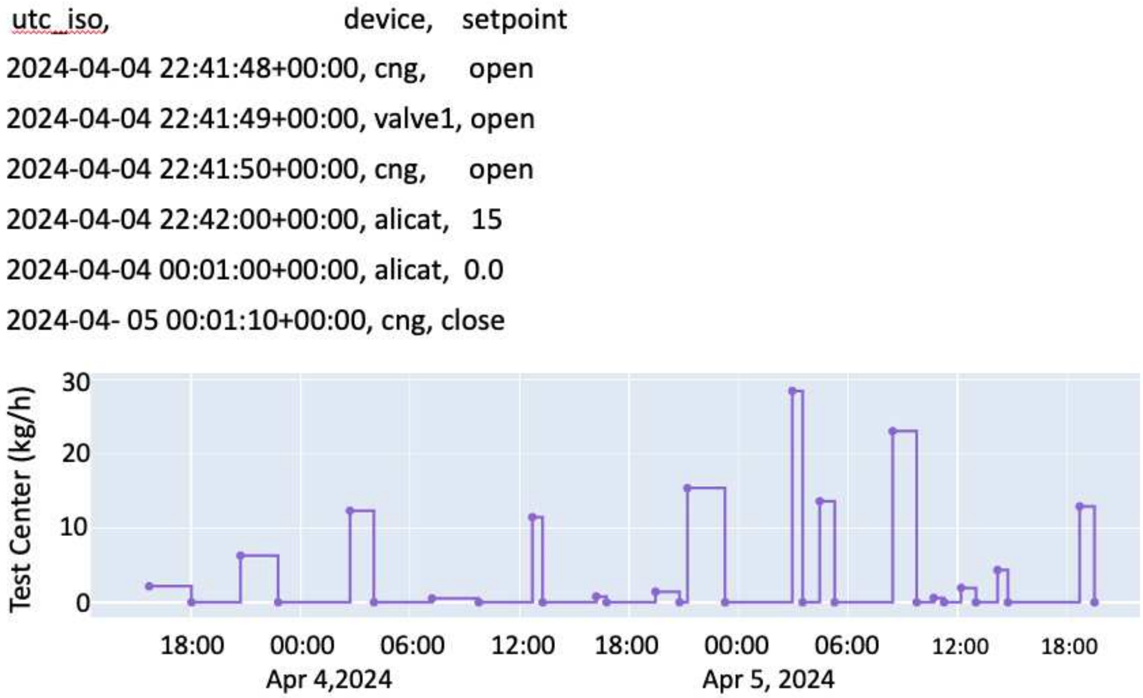

```
utc_iso,                          device,   setpoint
2024-04-04 22:41:48+00:00, cng,     open
2024-04-04 22:41:49+00:00, valve1, open
2024-04-04 22:41:50+00:00, cng,     open
2024-04-04 22:42:00+00:00, alicat,  15
2024-04-04 00:01:00+00:00, alicat,  0.0
2024-04- 05 00:01:10+00:00, cng, close
```

Figure 3.4: Example of generated test plan and time series plot of the generated test plan.

Figure 3.3 shows a case study where the test period was a 30 minute test indicating that the emissions start at (hh:57) accounting for the 3 minutes before test, while the test period starts at (hh:00). The test 1 was reported at (hh:00-hh:15) indicating that the first chunk 'Test 1' (the first message), was received at this time, and at (hh: 15-hh: 30) for 'Test2', while (hh: 31) the end of the emission accounts for the 1 min after the test was reported. To maintain accuracy in the analysis of this study, transition intervals in which the emission set point is temporarily set to zero before a new set point is established were excluded from the analysis. This exclusion ensures that the focus remains on continuous emissions at a constant emission rate per test period. The test was designed to understand the capabilities of the solution under a wide variety of environmental conditions. This is because we do not have control over these conditions, which is crucial to simulating real-world scenarios. For example, if the test is running at the same wind speed and direction over a while, say for four days, we pause the test and wait until the wind condition changes before we continue the testing to accommodate and simulate actual wind variation experienced in the real world scenario. During the testing period, the solution provided the detection reports according to the solution specification to the test center in one of four bins (0, 1, 2, and 3). Figure 3.6 shows the uniform distribution across each bin used to establish controlled release rates in this study. The lowest bin (emissions-Bin 0) was separated to differentiate the actual zero from the ones less than the minimum detection limit of 2.5 kgh^{-1}. Each emission rate setpoint duration and the subsequent zero-emission period were selected randomly but governed by rules to ensure that no gas was wasted after detection and that the testing period remained on track. To determine the composition of the natural gas used for the test, two laboratory tests were performed on two trailer fills during the test period, and an average of 95% CH_4 mole fraction was applied to the analysis of the performance data. Consequently, the test center representative randomly visited the site twice during the testing, which spans from March 12 to May 8, 2024 to ensure the integrity of the test, making sure that the site setup for the tests remains as expected. At the end of each test period, the data were reviewed, and the selection of tests per emission rate bin for the subsequent period was adjusted to close gaps in the emission rate distribution and increase the density of sample points around the emerging predicted reporting limit.

3.4 Performance Metrics

The basis of this study focuses on determining how well the solution performs by estimating the performance metrics (POR, False Positive Fraction (FPF), and False Negative Fraction (FNF)) [18, 34]. To do this, the test center compared the detection result generated by the solution with the ground truth of releases and a POR curve was created by plotting the detection report against the actual release rates. These metrics and the POR curve shows how well the solution performs under 'as tested' conditions and may not represent how well the solution performs when testing is carried out under different conditions. As such, it can only be said that the result from this study is applicable to the "as tested" conditions. The POR analysis in this study is based on the predefined minimum detection limit which defines bin 0 ($\leq 2.5\,\mathrm{kgh^{-1}}$). POR curve shows the likelihood that a solution can detect emissions at a specific magnitude. The FPF is the percentage of emissions that the solution incorrectly found while controlled releases were not taking place. The complement to this indicator is the FNF, which is the percentage of emissions that the solution failed to detect when controlled releases were occurring. In this study, the solution provided reports every 15-minutes in one of four "emissionsBins" (0, 1, 2, or 3) corresponding to estimated emission rates of $\leq 2.5, 2.5-7.5, 7.5-17.5,$ and $> 17.5\,\mathrm{kgh^{-1}}$ respectively. In a binary classification scheme, the Test Center was told to interpret the results in bin 0 ($\leq 2.5\,\mathrm{kgh^{-1}}$) as "negative" and reports in bins 1, 2, or 3 ($> 2.5\,\mathrm{kgh^{-1}}$) as "positive". The "Test Center" was not given any numerical indicators of suspected emissions or uncertainties (e.g $3.6\,\mathrm{kgh^{-1}} \pm 1.2\,\mathrm{kgh^{-1}}$), and all emissions $\leq 2.5\,\mathrm{kgh^{-1}}$ are included in the lowest reporting bin; that is, there is no difference between an emission rate of 0 $\mathrm{kgh^{-1}}$and 2.5 $\mathrm{kgh^{-1}}$.

3.5 Test Configuration

This study is solely based on simulating a typical wellhead test structure. The test site consists of the deployed solution to be evaluated located at 52 feet from the controlled release point and approximately 6.5 feet above grade. The layout shown in Figure 3.5 illustrates the schematic of the green field site close to an active O&G production area used in this study to solely simulate a typical wellhead test configuration (see Figure A.1 for the actual site deployment) in south Texas. From the gas release point, there is a pig launcher and receiver that is used once a month located approximately 30 meters away. During the testing phase, pigging occurred once. As such, it was ensured that controlled releases were not carried out at this time to ensure that the pigging event did not influence the solution's detection performance.

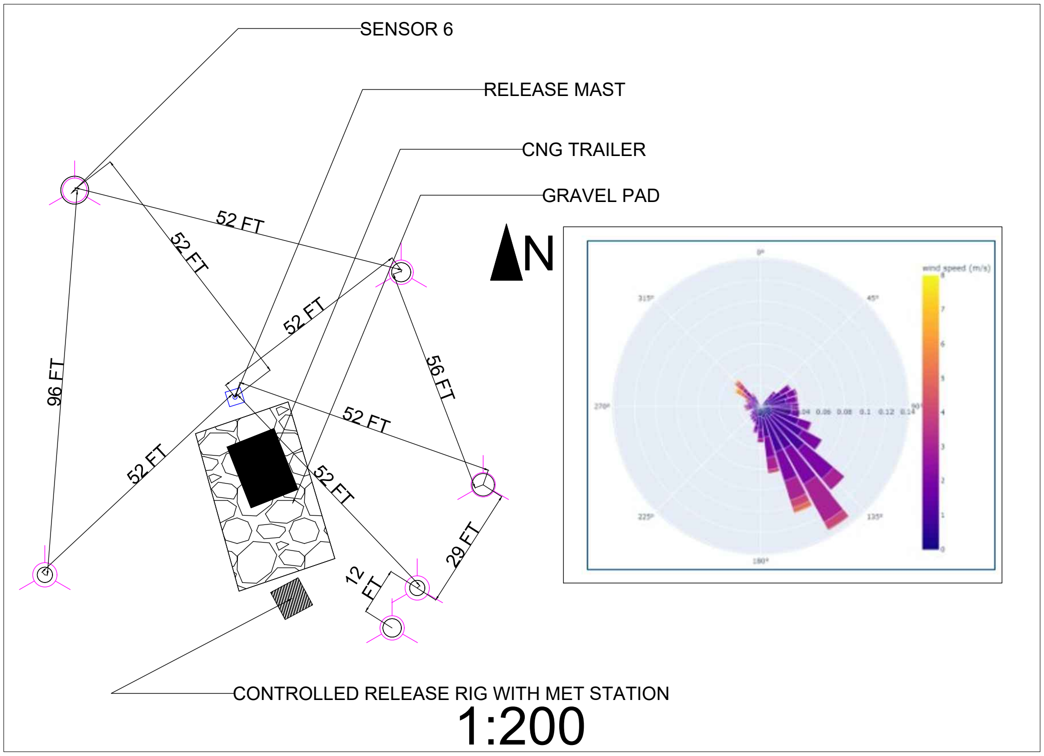

Figure 3.5: Test site layout representation showing the CNG trailer, gas release mast, gravel pad, CRR with MET station, and six sensor nodes for the solution under test.

In the solution setup, Meteorological (MET) station is installed on two of the six sensors. There is also an independent MET station mounted on the CRR at approximately

10 feet above grade while the CNG trailer which supplies the CRR gas throughout the testing period is located between CRR and gas release mast.

3.6 Input Specification

In this study, the Message Queuing Telemetry Transport (MQTT) is used for receiving detection report from the solution center, in the format: "emissionsBin": x. Here, x represent an "emissionsBin" 0, 1, 2, or 3. While this format does not provide any timestamp information, nearly all of the messages were received within the second of the reporting interval, with a few being delayed by an extra one to two seconds. The binary classification scheme in this study is define by taking the report of "emissionsBin": 0 as no emission, or emissions detected below the threshold ($\leq$ 2.5 kgh^{-1}), while that of "emissionsBin": 1, "emissionsBin": 2, and "emissionsBin": 3 is reported as detected emission or emissions detected above the threshold ($>$ 2.5 kgh^{-1}) respectively.

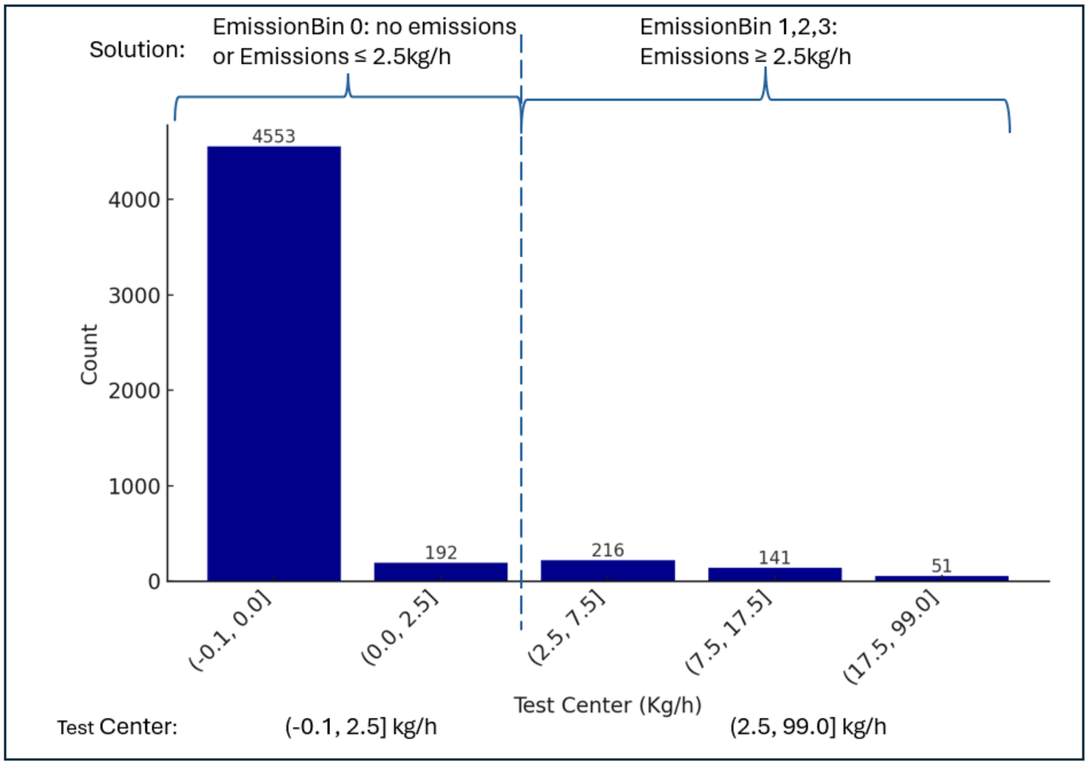

Figure 3.6: Input specification for solution and test center. Test center lower bin limit is negative to include 0 kgh^{-1}within the interval. Test center upper bin limit is 99.0 to close the interval with a reasonable "large" value > 17.5 kgh^{-1}.

Thus, Figure 3.6 shows that the controlled release test input specification simulates the real world scenario by ensuring that there is a limited number of actual leaks during the test period, indicating that out of the 5153 tests there were 408 (7.9 %) actual leaks.

Chapter 4

Results and Discussion

To begin with, a time series plot of the generated test plan was created with collected data to check for completeness and accuracy. Figure 4.1 shows an example of the solution-reported detection for a twelve-hour test period out of the entire testing period. It illustrates how the data was overlayed on the actual releases to begin analyzing the performance of the solution. From the figure, it is seen that, in section A and D, the solution correctly detects emissions for the period while the setpoint was greater than the minimum detection limit ($> 2.5\,\mathrm{kgh^{-1}}$). Region B shows that the solution detects emission two out of six times when the setpoint is greater than the minimum detection limit ($> 2.5\,\mathrm{kgh^{-1}}$). In section C, the solution correctly reported that there were no active releases, and section E illustrated two periods when the setpoint was less than or equal to the minimum detection limit ($\leq 2.5\,\mathrm{kgh^{-1}}$).

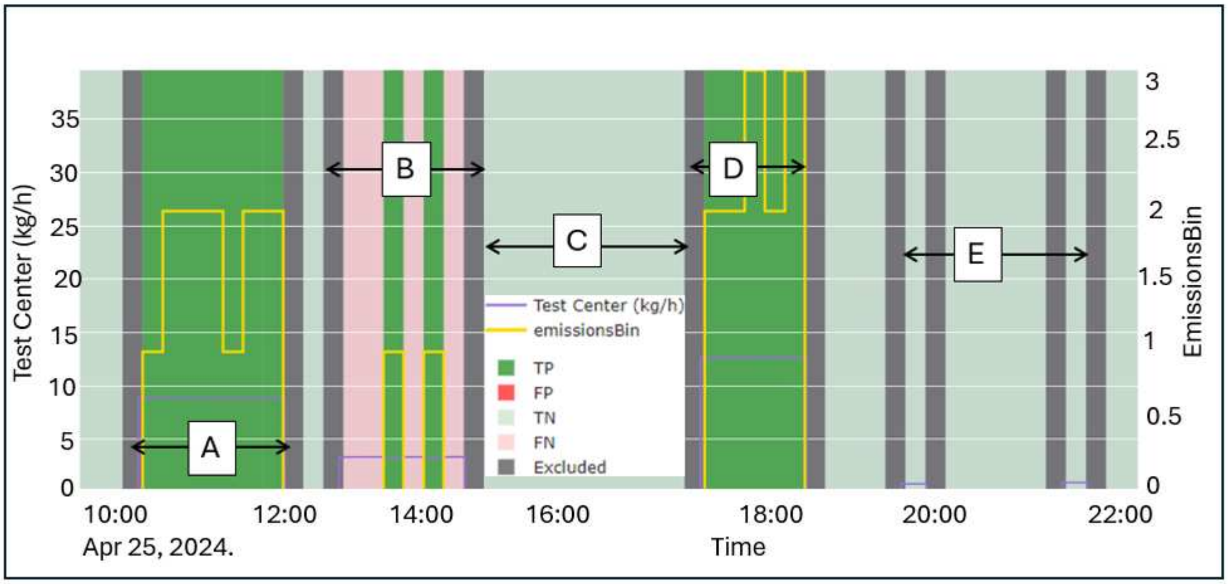

Figure 4.1: Example time series plot showing the overlay of the reported detection on the generated test plan during the single-blind, controlled-release testing.

4.1 Binary Detection Analysis

For this particular solution, an anticipated future enhancement is the ability to categorize the test into discrete emissions bins. However, for this testing in the preliminary analysis and the preliminary tests, detection of CH$_4$ emission is only considered, meaning yes or no (1, or 0), and not quantification by bin.

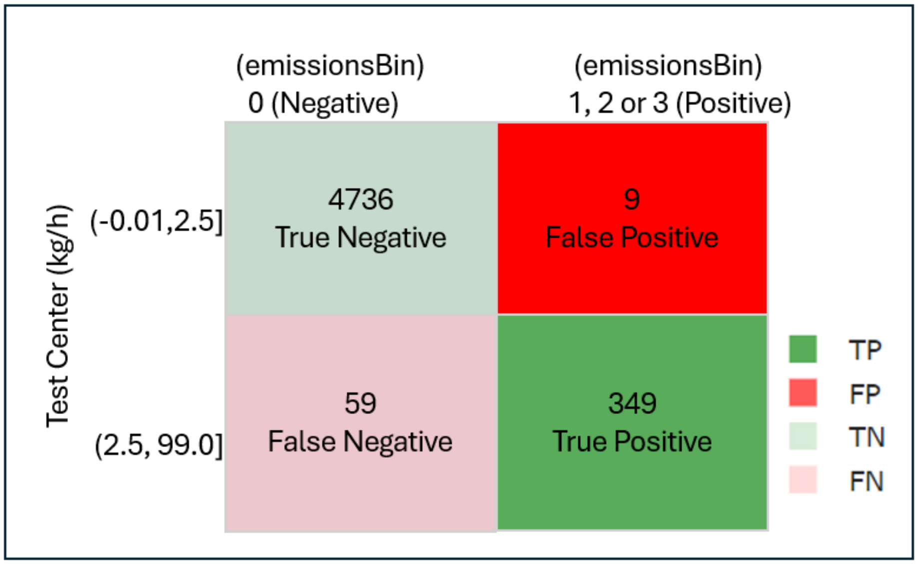

Test Center (kg/h)	(emissionsBin) 0 (Negative)	(emissionsBin) 1, 2 or 3 (Positive)
(-0.01,2.5]	4736 True Negative	9 False Positive
(2.5, 99.0]	59 False Negative	349 True Positive

🟩 TP
🟥 FP
🟩 TN
🟥 FN

Figure 4.2: Confusion matrix showing solution detection performance.

Upon the completion of the test, the primary metrics shown in Table 4.1 considered in this study were calculated and the solution reported 4,553 15-minute chunks, where emissions were not detected, and 600, 15-minute chunks, where emission were actually detected based on the predefined test protocol. For 349 times out of 408 intervals, the solution detected emissions from the controlled releases and reported it in the positive emission bin (emissionsBin 1,2, or 3) which account for 86 % TPR. Thus, the solution reported negative (emissionsBin 0) in 4736 of 4,745 intervals, when the emission rate is less or equal to 2.5 kgh^{-1}, accounting for 99.8 % True Negative Rate (TNR). It erroneously reported 9 positives out of 4745 emission rate less than or equal to 2.5 kgh^{-1}which equate to 0.2 % False Positive Rate (FPR). For the FNR, it erroneously reported negative when emission rates are greater than 2.5 kgh^{-1}, 59 out of 408 intervals accounting for 14 % FNR. This study's analysis includes all reporting intervals, including those without active releases from the test center. If the analysis were to only include reporting intervals with active releases, the solution accurately reported negative (in emissionsBin 0) for 183 out of 192 intervals, resulting to a 95 % TNR, and emissions were erroneously reported positive (in emissionsBin 1, 2, or 3) for the remaining 9 tests in this category, at a FPR of 5 %.

Table 4.1: Parametric table showing the solution's detection performance.

Parameters	Values
True Negative Rate	0.998
False Positive Rate	0.002
False Negative Rate	0.145
True Positive Rate	0.855
Negative Predictive Value	0.988
False Discovery Rate	0.025
False Omission Rate	0.012
Positive Predictive Value	0.975
Accuracy	0.987

Overall, from Table 4.1, considering the high TNR (0.998), Positive Predictive Value (PPV) (0.975), and Accuracy (0.987) the system performs very well. The low FPR (0.002) and False Discovery Rate (FDR) (0.025) indicate that false alarms are not very common. However, there is potential for improvement in terms of lowering missed detections because the FNR (0.145) is high (see Appendix C for details).

4.1.1 Probability of Reporting (POR)

The POR shown in Figure 4.3 illustrates positive indication. POR curve shows the likelihood that a solution can detect emissions at a specific magnitude. This plot was generated with the 5,153 reporting intervals in the single-blind controlled release test carried out in this study. The reported data generated was plotted against the ground truth emission rates and a logistic regression curve was fit as shown in Figure 4.3.

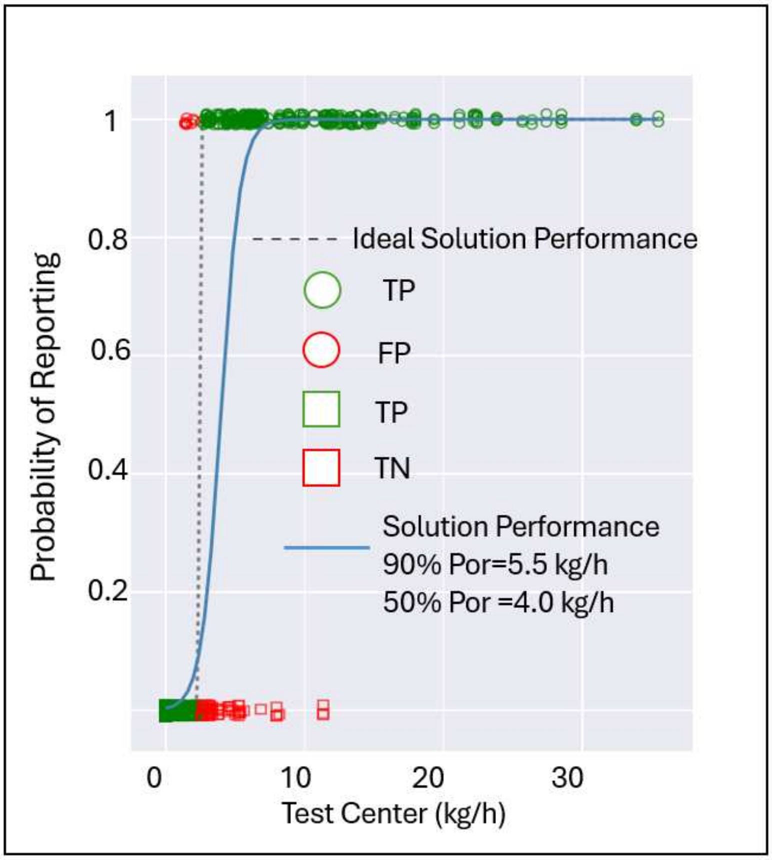

Figure 4.3: Probability of reporting (POR). Ideal performance is shown by the dashed line, actual performance is shown by the solid line.

From Figure 4.3 the ideal performance that presents how the solution is expected to behave under perfect conditions is illustrated by the dotted line, actual performance is shown by the solid line and green indicates the correct reported emissions, while red indicates the incorrect reported emission. The emission rates greater than 2.5 kgh^{-1}would always be recorded as "positive" (100 percent likelihood), whereas emission rates less than 2.5 kgh^{-1}(including 0 kgh^{-1}) would never be reported as "positive" (0 percent probability). In Figure 4.3, the blue line illustrates how the solution performance deviates from the ideal case study, illustrating the presence of FPs and FNs in the reported results. Based on this curve we see that the solution has a 10 % possibility of reporting emissions at 2.5 kgh^{-1}, a 50 % probability of reporting emissions at 4 kgh^{-1}, a 90 % probability of reporting emissions at 5.5 kgh^{-1}. For all the single-blind controlled release tests carried out in this study, the solution always produced positive results for emission rates greater than 11.3 kgh^{-1}and never reported positive results for less than 1.4 kgh^{-1}emission rates. Additionally, the solution did not report positive during any intervals without controlled releases.

4.1.2 Wind Bin Distributions During Test

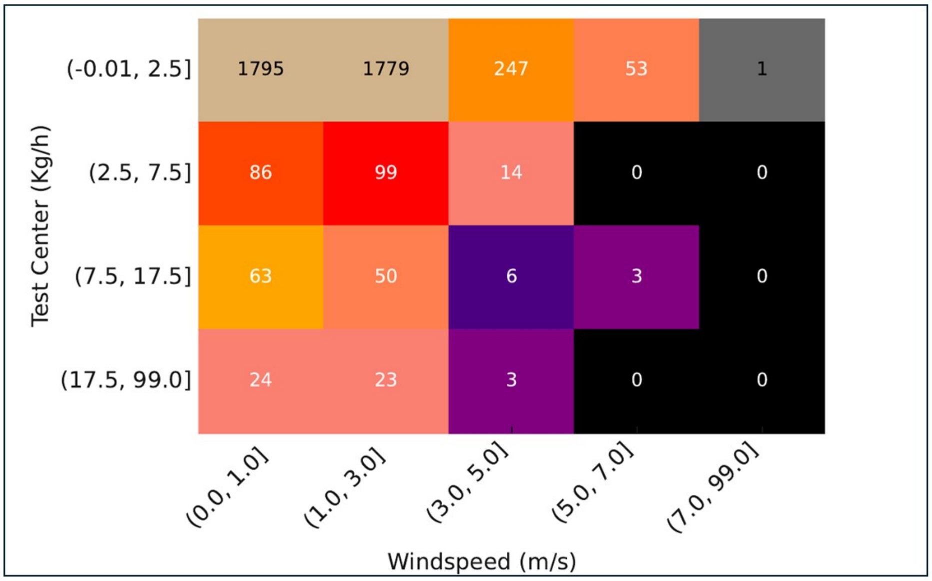

Figure 4.4: Count of tests per emission rate bin vs wind speed bin during the test period.

Figure 4.4 shows the distribution of wind speed against emission rate bin. Many tests were conducted with average 15-minute wind speeds below 5 ms^{-1}. Three of the tests had active emissions (all in one bin) with average wind speeds greater than 5 ms^{-1}. The remaining 53 test intervals were periods with 0 kgh^{-1}emission rates.

Table 4.2: Solution performance for increasing wind speeds.

Wind Speed (m/s): (Numbers of tests)							
Parameter	All: (5153)	<1: (2875)	>1: (2278)	[1.0, 2.0): (1331)	>2: (957)	[2.0, 3.0): (620)	>3: (327)
90 % POR (kgh)	5.5	6.5	4.4	4.8	3.8	3.2	4.0
50 % POR (kgh)	4.0	4.6	3.3	3.5	3.0	3.0	3.0
True positive rate	0.86	0.833	0.88	0.869	0.90	0.886	0.923
False negative rate	0.14	0.167	0.12	0.131	0.10	0.114	0.077
False positive rate	0.002	0.002	0.002	0.003	0	0	0
True negative rate	0.998	0.998	0.998	0.997	1	1	1
Positive predictive value	0.975	0.972	0.978	0.967	1	1	1
False discovery rate	0.025	0.028	0.022	0.033	0	0	0
False omission rate	0.012	0.013	0.011	0.015	0.01	0.007	0.007
Negative predictive value	0.988	0.987	0.989	0.985	0.99	0.993	0.993
Accuracy	0.978	0.986	0.988	0.983	0.99	0.994	0.994

The performance of the solution appeared to improve as wind speeds increased. Grouping test results for all wind speeds, and comparing to tests with different windspeed conditions, the performance of the solution improved continuously as shown in Table 4.2. Above 3.0 ms^{-1}, there were not enough samples to provide a meaningful insight.

During the single-blind controlled release test period, the wind direction was predominantly south-east as illustrated in Figure 3.5. Consequently, as it is typical for remote downwind sensor arrays, the study thus demonstrates that the wind speed influenced the solution performance, with the solution performance improving as the wind speed increases. The study shows significant improvement when the wind speed was greater than 3 ms^{-1}for the 327 reporting intervals; the solution performance begins to approach ideal state and the FNR improved from 0.014 to 0.077. FNR is an important consideration in evaluating the performance of the solution under varying wind speeds. A FNR refers to a release event that occurs but is not detected by the system. A distinct pattern emerged from the analysis of the test data: as wind speed increases, the FNR decreases. The FNR for all the test data was 0.141, and at wind speeds less than 1.0 ms^{-1}it increased to 0.167. For wind speeds between 1.0 $ms^{-1}$and 2.0 ms^{-1}, this value decreased to 0.131; for wind speeds between 2.0 $ms^{-1}$and 3.0 ms^{-1}it decreased to 0.114; and at greater than 3.0 ms^{-1}, it reached its lowest value of 0.077. According to this pattern, low windspeed conditions lead to less plume transport and less interaction between the sensor's detecting path and the methane plume. Higher wind speeds, on the other hand, improve plume advection and raise the possibility of detection. These results highlight the need of taking environmental factors into account when evaluating the effectiveness of solutions and recommend that system optimization take wind condition variability especially the difficulties presented by low-wind scenarios into account. The performance shows 99.4 % accuracy, the 90 % POR improved from 5.5 to 4.0 and at 50 % POR from 4.0 to 3.0. In these wind conditions, the solution consistently reported positive for emission rates greater than 3.2 $kgh^{-1}$and never reported "positive" for rates less than 3.1 kgh^{-1}under these wind conditions.

4.2 Uncertainty

4.2.1 Mass Flow Rate Uncertainty

During the single-blind controlled release tests, natural gas was released using a mass flow controller with a full-scale capacity of $55.93\,\mathrm{kg\,h^{-1}}$ (equivalent to 1300 SLPM). According to the manufacturer [78], the flow controller accuracy is specified as

$$\pm(0.8\% \text{ of reading} + 0.2\% \text{ of full scale})$$

$$\pm(0.8\% \text{ of reading} + 0.2\% \times 55.93) = \pm(0.8\% \text{ of reading} + 0.1119)$$

Example 1 – At a release rate of $12\,\mathrm{kg\,h^{-1}}$**:**

$$\begin{aligned}\text{Uncertainty} &= \pm(0.008 \times 12 + 0.1119)\\ &= \pm(0.096 + 0.1119)\\ &= \pm 0.2079\ \mathrm{kg\,h^{-1}}\end{aligned}$$

Example 2 – At a release rate of $32\,\mathrm{kg\,h^{-1}}$**:**

$$\begin{aligned}\text{Uncertainty} &= \pm(0.008 \times 32 + 0.1119)\\ &= \pm(0.256 + 0.1119)\\ &= \pm 0.3679\ \mathrm{kg\,h^{-1}}\end{aligned}$$

4.2.2 Wind Speed Uncertainty

The wind speed accuracy is specified as ±5 % at 10 $\mathrm{ms^{-1}}$, measured at four angles. This means that at a wind speed of 10 $\mathrm{ms^{-1}}$, the expected measurement uncertainty is ± 0.5 $\mathrm{ms^{-1}}$. The sensor's resolution is 0.1 $\mathrm{ms^{-1}}$, and the specified wind speed range is from 0 to 40 $\mathrm{ms^{-1}}$

For wind speeds lower than 10 $\mathrm{ms^{-1}}$, the absolute uncertainty would be proportionally less. However, the manufacturer does not provide explicit accuracy specifications for these lower wind speeds. Therefore, while the relative percentage error remains at 5%, the absolute error decreases with lower wind speeds.

Based on the dataset from this study, the wind speed was always less than 10 ms^{-1}, with most of the tests having wind speeds less than 5 ms^{-1}, and three of the tests having wind speeds between 5 $ms^{-1}$and 7 ms^{-1}.

Although the wind speed measurements were not utilized by the solution itself, they were instrumental in planning the test matrix to ensure a diverse range of conditions. In the subsequent analysis, these measurements were used to categorize results into discrete wind speed bins (e.g., < 1 ms^{-1}, 1–2 ms^{-1}, etc.). It is recognized that measurement uncertainty introduces potential error in the binning process. Based on the resolution and stated accuracy of the measurement instrument, a conservative estimate of the uncertainty at the lowest bin threshold (1 ms^{-1}) is $\pm$ 0.1 ms^{-1}. This level of uncertainty is considered acceptable for the purposes of evaluating solution performance trends across wind speed categories. While this may result in limited misclassification at bin boundaries, the uncertainty is assumed to follow a normal distribution, thus minimizing the likelihood of systematic bias in the grouping. Consequently, the overall impact on the analysis and conclusions is expected to be negligible.

Chapter 5

Conclusion

A CRR was developed and constructed which allowed for remote test execution around-the-clock. A series of independent single-blind tests were conducted to evaluate the detection and quantification capabilities of CM CH_4 solution. The CRR allowed the Test Center to supply active gas releases for 600 distinct test periods with 157 fixed setpoints that ranged from 15 minutes to 3 hours and from 0.5 $kgh^{-1}$to 37.5 kgh^{-1}. Considering every 15-minute chunk (all test points included), TPR and FNR for the solution were 86 % and 14 %, respectively, while TNR and FPR were 99.8 % and 0.2 %, respectively. These same metrics were and 95 % and 5 %, respectively, when only active controlled release periods were included (15-minute chunk with emission occuring). The solution never produced a "positive" result when emission rates were less than 1.4 kgh^{-1}, and always reported “positive” when emission rates were greater than 11.3 kgh^{-1}. The solution’s 50 % probability of reporting was 3.8 kgh^{-1}, and its 90 % likelihood of reporting during the full testing time was 5.5 kgh^{-1}. The performance of the solution increased with increasing wind speeds over the testing range, as is the case with most of the fixed point, remote sensors. With average wind speeds greater than 2 ms^{-1}, the solution’s performance almost perfectly satisfies the ideal perfomance specified in its design target.

Bibliography

[1] Intergovernmental Panel On Climate Change (Ipcc), Climate Change 2021 – The Physical Science Basis: Working Group I Contribution to the Sixth Assessment Report of the Intergovernmental Panel on Climate Change, 1st Edition, Cambridge University Press, 2023. `doi:10.1017/9781009157896`.
URL https://www.cambridge.org/core/product/identifier/9781009157896/type/book

[2] Z. Chen, S. H. El Abbadi, E. D. Sherwin, P. M. Burdeau, J. S. Rutherford, Y. Chen, Z. Zhang, A. R. Brandt, Comparing continuous methane monitoring technologies for high-volume emissions: A single-blind controlled release study, ACS ES&T Air (2024).

[3] Methane | Vital Signs, acessed 2024-10-23.
URL https://climate.nasa.gov/vital-signs/methane?intent=121

[4] O. US EPA, Importance of Methane, accessed April 17, 2025 (Jan. 2016).
URL https://www.epa.gov/gmi/importance-methane

[5] D. J. Jacob, D. J. Varon, D. H. Cusworth, P. E. Dennison, C. Frankenberg, R. Gautam, L. Guanter, J. Kelley, J. McKeever, L. E. Ott, et al., Quantifying methane emissions from the global scale down to point sources using satellite observations of atmospheric methane, Atmospheric Chemistry and Physics 22 (14) (2022) 9617–9646.

[6] D. J. Varon, D. Jervis, J. McKeever, I. Spence, D. Gains, D. J. Jacob, High-frequency monitoring of anomalous methane point sources with multispectral sentinel-2 satellite observations, Atmospheric Measurement Techniques 14 (4) (2021) 2771–2785.

[7] C. UNEP, Global methane assessment: benefits and costs of mitigating methane emissions, United Nations Environment Programme (UNEP)(ed). Nairobi (2021).

[8] M. Saunois, A. R. Stavert, B. Poulter, P. Bousquet, J. G. Canadell, R. B. Jackson, P. A. Raymond, E. J. Dlugokencky, S. Houweling, P. K. Patra, P. Ciais, V. K. Arora, D. Bastviken, P. Bergamaschi, D. R. Blake, G. Brailsford, L. Bruhwiler, K. M. Carlson, M. Carrol, S. Castaldi, N. Chandra, C. Crevoisier, P. M. Crill, K. Covey, C. L. Curry, G. Etiope, C. Frankenberg, N. Gedney, M. I. Hegglin, L. Höglund-Isaksson, G. Hugelius, M. Ishizawa, A. Ito, G. Janssens-Maenhout, K. M. Jensen, F. Joos, T. Kleinen, P. B. Krummel, R. L. Langenfelds, G. G. Laruelle, L. Liu, T. Machida, S. Maksyutov, K. C. McDonald, J. McNorton, P. A. Miller, J. R. Melton, I. Morino, J. Müller, F. Murguia-Flores, V. Naik, Y. Niwa, S. Noce, S. O'Doherty, R. J. Parker, C. Peng, S. Peng, G. P. Peters, C. Prigent, R. Prinn, M. Ramonet, P. Regnier, W. J. Riley, J. A. Rosentreter, A. Segers, I. J. Simpson, H. Shi, S. J. Smith, L. P. Steele, B. F. Thornton, H. Tian, Y. Tohjima, F. N. Tubiello, A. Tsuruta, N. Viovy, A. Voulgarakis, T. S. Weber, M. van Weele, G. R. van der Werf, R. F. Weiss, D. Worthy, D. Wunch, Y. Yin, Y. Yoshida, W. Zhang, Z. Zhang, Y. Zhao, B. Zheng, Q. Zhu, Q. Zhu, Q. Zhuang, The Global Methane Budget 2000–2017, Earth System Science Data 12 (3) (2020) 1561–1623, publisher: Copernicus GmbH. `doi:10.5194/essd-12-1561-2020`.
URL https://essd.copernicus.org/articles/12/1561/2020/

[9] A. J. Marchese, T. L. Vaughn, D. J. Zimmerle, D. M. Martinez, L. L. Williams, A. L. Robinson, A. L. Mitchell, R. Subramanian, D. S. Tkacik, J. R. Roscioli, et al., Methane emissions from united states natural gas gathering and processing, Environmental science & technology 49 (17) (2015) 10718–10727.

[10] O. US EPA, Overview of Greenhouse Gases (Dec. 2015).
URL https://www.epa.gov/ghgemissions/overview-greenhouse-gases(accessedonNovember720

[11] C. Ilonze, J. Wang, A. P. Ravikumar, D. Zimmerle, Methane quantification performance of the quantitative optical gas imaging (qogi) system using single-blind controlled release assessment, Sensors 24 (13) (2024) 4044.

[12] J. L. Wang, W. S. Daniels, D. M. Hammerling, M. Harrison, K. Burmaster, F. C. George, A. P. Ravikumar, Multiscale methane measurements at oil and gas facilities reveal necessary frameworks for improved emissions accounting, Environmental science & technology 56 (20) (2022) 14743–14752.

[13] P. Smith, D. Reay, J. Smith, Agricultural methane emissions and the potential formitigation, Philosophical Transactions of the Royal Society A 379 (2210) (2021) 20200451.

[14] O. US EPA, Methane Emissions (Jan. 2025).
URL https://www.epa.gov/ghgemissions/methane-emissions

[15] Optical Methods of Methane Detection.
URL https://www.mdpi.com/1424-8220/23/5/2834

[16] T. Kormi, N. B. H. Ali, T. Abichou, R. Green, Estimation of landfill methane emissions using stochastic search methods, Atmospheric Pollution Research 8 (4) (2017) 597–605.

[17] F. Cheptonui, E. Emerson, C. Ilonze, R. Day, E. Levin, D. Fleischmann, R. Brouwer, D. Zimmerle, Assessing the performance of emerging and existing continuous monitoring solutions under a single-blind controlled testing protocol (2024).

[18] C. Ilonze, E. Emerson, A. Duggan, D. Zimmerle, Assessing the progress of the performance of continuous monitoring solutions under a single-blind controlled testing protocol, Environmental Science & Technology (2024). `doi:10.1021/acs.est.3c08511`.
URL https://pubs.acs.org/doi/10.1021/acs.est.3c08511

[19] D. H. Cusworth, R. M. Duren, A. K. Thorpe, W. Olson-Duvall, J. Heckler, J. W. Chapman, M. L. Eastwood, M. C. Helmlinger, R. O. Green, G. P. Asner, P. E. Dennison, C. E. Miller, Intermittency of Large Methane Emitters in the Permian Basin, Environmental Science & Technology Letters 8 (7) (2021) 567–573, publisher: American

Chemical Society. `doi:10.1021/acs.estlett.1c00173`.
URL https://doi.org/10.1021/acs.estlett.1c00173

[20] L. M. Golston, N. F. Aubut, M. B. Frish, S. Yang, R. W. Talbot, C. Gretencord, J. McSpiritt, M. A. Zondlo, Natural gas fugitive leak detection using an unmanned aerial vehicle: Localization and quantification of emission rate, Atmosphere 9 (9) (2018) 333.

[21] A. P. Ravikumar, S. Sreedhara, J. Wang, J. Englander, D. Roda-Stuart, C. Bell, D. Zimmerle, D. Lyon, I. Mogstad, B. Ratner, et al., Single-blind inter-comparison of methane detection technologies–results from the stanford/edf mobile monitoring challenge, Elem Sci Anth 7 (2019) 37.

[22] N. Blume, T. G. Pernini, J. T. Dobler, T. S. Zaccheo, D. McGregor, C. Bell, Single-blind detection, localization, and quantification of methane emissions using continuous path-integrated column measurements, Elem Sci Anth 12 (1) (2024) 00022. `doi:10.1525/elementa.2024.00022`.
URL https://online.ucpress.edu/elementa/article/12/1/00022/202933/Single-blind-detection-localization-and

[23] C. E. Kemp, A. P. Ravikumar, New Technologies Can Cost Effectively Reduce Oil and Gas Methane Emissions, but Policies Will Require Careful Design to Establish Mitigation Equivalence, Environmental Science & Technology 55 (13) (2021) 9140–9149, publisher: American Chemical Society. `doi:10.1021/acs.est.1c03071`.
URL https://doi.org/10.1021/acs.est.1c03071

[24] X. Yang, E. Kuru, X. Zhang, S. Zhang, R. Wang, J. Ye, D. Yang, J. J. Klemeš, B. Wang, Direct measurement of methane emissions from the upstream oil and gas sector: Review of measurement results and technology advances (2018–2022), Journal of Cleaner Production 414 (2023) 137693.

[25] M. Wik, B. F. Thornton, D. Bastviken, J. Uhlbäck, P. M. Crill, Biased sampling of methane release from northern lakes: A problem for extrapolation, Geophysical Research Letters 43 (3) (2016) 1256–1262, _eprint: https://onlinelibrary.wiley.com/doi/pdf/10.1002/2015GL066501. `doi:10.1002/2015GL066501`.
URL https://onlinelibrary.wiley.com/doi/abs/10.1002/2015GL066501

[26] G. Plant, E. A. Kort, A. R. Brandt, Y. Chen, G. Fordice, A. M. Gorchov Negron, S. Schwietzke, M. Smith, D. Zavala-Araiza, Inefficient and unlit natural gas flares both emit large quantities of methane, Science 377 (6614) (2022) 1566–1571, publisher: American Association for the Advancement of Science. `doi:10.1126/science.abq0385`.
URL https://www.science.org/doi/full/10.1126/science.abq0385

[27] D. T. Allen, F. J. Cardoso-Saldaña, Y. Kimura, Variability in Spatially and Temporally Resolved Emissions and Hydrocarbon Source Fingerprints for Oil and Gas Sources in Shale Gas Production Regions, Environmental Science & Technology 51 (20) (2017) 12016–12026, publisher: American Chemical Society. `doi:10.1021/acs.est.7b02202`.
URL https://doi.org/10.1021/acs.est.7b02202

[28] R. E. Day, E. Emerson, C. Bell, D. Zimmerle, Point sensor networks struggle to detect and quantify short controlled releases at oil and gas sites, Sensors 24 (8) (2024) 2419.

[29] C. Bell, J. Rutherford, A. Brandt, E. Sherwin, T. Vaughn, D. Zimmerle, Single-blind determination of methane detection limits and quantification accuracy using aircraft-based LiDAR, Elementa: Science of the Anthropocene 10 (1) (2022) 00080. `doi:10.1525/elementa.2022.00080`.
URL https://doi.org/10.1525/elementa.2022.00080

[30] C. S. Bell, T. L. Vaughn, D. Zimmerle, S. C. Herndon, T. I. Yacovitch, G. A. Heath, G. Pétron, R. Edie, R. A. Field, S. M. Murphy, et al., Comparison of methane emission estimates from multiple measurement techniques at natural gas production pads, Elem Sci Anth 5 (2017) 79.

[31] What is a TDLAS Methane Sensor, Understanding the Technology and Its Applications.
URL https://www.winsen-sensor.com/knowledge/what-is-a-tdlas-methane-sensor.html

[32] E. D. Sherwin, Y. Chen, A. P. Ravikumar, A. R. Brandt, Single-blind test of airplane-based hyperspectral methane detection via controlled releases, Elementa: Science of the Anthropocene 9 (1) (2021) 00063. `doi:10.1525/elementa.2021.00063`.
URL https://online.ucpress.edu/elementa/article/9/1/00063/116576/Single-blind-test-of-airplane-based-hyperspectral

[33] C. Bell, D. Zimmerle, METEC controlled test protocol: continuous monitoring emission detection and quantification, medium: Testing,reports (Jun. 2022). `doi:10.25675/10217/235364`.
URL https://mountainscholar.org/handle/10217/235364

[34] C. Bell, C. Ilonze, A. Duggan, D. Zimmerle, Performance of Continuous Emission Monitoring Solutions under a Single-Blind Controlled Testing Protocol, Environmental science & technology 57 (Mar. 2023). `doi:10.1021/acs.est.2c09235`.

[35] T. L. Vaughn, C. S. Bell, C. K. Pickering, S. Schwietzke, G. A. Heath, G. Pétron, D. J. Zimmerle, R. C. Schnell, D. Nummedal, Temporal variability largely explains top-down/bottom-up difference in methane emission estimates from a natural gas production region, Proceedings of the National Academy of Sciences 115 (46) (2018) 11712–11717.

[36] 40 CFR Part 60 Subpart OOOOb – Standards of Performance for Crude Oil and Natural Gas Facilities for Which Construction, Modification or Reconstruction Commenced After December 6, 2022.
URL https://www.ecfr.gov/current/title-40/part-60/subpart-OOOOb

[37] T. Aldhafeeri, M.-K. Tran, R. Vrolyk, M. Pope, M. Fowler, A review of methane gas detection sensors: Recent developments and future perspectives, Inventions 5 (3) (2020) 28.

[38] R. Tu, J. Gu, Y. Zeng, X. Zhou, K. Yang, J. Jing, Z. Miao, J. Yang, Development and validation of a tunable diode laser absorption spectroscopy system for hot gas flow and small-scale flame measurement, Sensors 22 (17) (2022) 6707.

[39] X. Liu, Y. Ma, Tunable Diode Laser Absorption Spectroscopy Based Temperature Measurement with a Single Diode Laser Near 1.4 µm, Sensors 22 (16) (2022) 6095, number: 16 Publisher: Multidisciplinary Digital Publishing Institute. `doi:10.3390/s22166095`.
URL https://www.mdpi.com/1424-8220/22/16/6095

[40] What is TDLAS: A Comprehensive Guide to Tunable Diode Laser Absorption Spectroscopy.
URL https://www.winsen-sensor.com/knowledge/what-is-tdlas.html

[41] W.-H. Zhang, W.-Q. Wang, L. Zhang, X. Dai, X.-L. Liu, L. Jiang, Methane gas detection based on tunable diode laser absorption spectroscopy and optical fiber sensing, in: 2014 7th International Conference on Intelligent Computation Technology and Automation, IEEE, 2014, pp. 365–368.

[42] S. Lin, J. Chang, J. Sun, P. Xu, Improvement of the detection sensitivity for tunable diode laser absorption spectroscopy: a review, Frontiers in Physics 10 (2022) 853966.

[43] J. Xia, C. Feng, F. Zhu, S. Ye, S. Zhang, A. Kolomenskii, Q. Wang, J. Dong, Z. Wang, W. Jin, et al., A sensitive methane sensor of a ppt detection level using a mid-infrared interband cascade laser and a long-path multipass cell, Sensors and actuators B: chemical 334 (2021) 129641.

[44] J. Jiang, M. Zhao, G.-M. Ma, H.-T. Song, C.-R. Li, X. Han, C. Zhang, Tdlas-based detection of dissolved methane in power transformer oil and field application, IEEE Sensors Journal 18 (6) (2018) 2318–2325.

[45] J. Fraden, J. King, Handbook of modern sensors: physics, designs, and applications, Vol. 3, Springer, 2004.

[46] W. Dong, Y. Sugai, Y. Wang, H. Zhang, X. Zhang, K. Sasaki, Experimental study on enhanced methane detection using an mems-pyroelectric sensor integrated with a wavelet algorithm, ACS omega 9 (18) (2024) 19956–19967.

[47] L. Jun, T. Qiulin, Z. Wendong, X. Chenyang, G. Tao, X. Jijun, Miniature low-power ir monitor for methane detection, Measurement 44 (5) (2011) 823–831.

[48] C.-D. Kohl, T. Wagner, Gas sensing fundamentals, Vol. 15, Springer, 2014.

[49] F. Bíró, C. Dücső, G. Z. Radnóczi, Z. Baji, M. Takács, I. Bársony, Ald nano-catalyst for micro-calorimetric detection of hydrocarbons, Sensors and Actuators B: Chemical 247 (2017) 617–625.

[50] N.-H. Park, T. Akamatsu, T. Itoh, N. Izu, W. Shin, Calorimetric thermoelectric gas sensor for the detection of hydrogen, methane and mixed gases, Sensors 14 (5) (2014) 8350–8362.

[51] R. E. Cavicchi, Calorimetric sensors, Chemical Sensors; National Institute of Standards and Technology: Gaithersburg, MD, USA (2011) 287–320.

[52] P. Shankar, J. B. B. Rayappan, Gas sensing mechanism of metal oxides: The role of ambient atmosphere, type of semiconductor and gases-a review, Sci. Lett. J 4 (4) (2015) 126.

[53] R. Chen, S. Lin, Z. Wang, Y. Xia, L. Xiang, Metal oxide semiconductor based methane sensing, Carbon Future (2025).

[54] Z. Li, H. Li, Z. Wu, M. Wang, J. Luo, H. Torun, P. Hu, C. Yang, M. Grundmann, X. Liu, et al., Advances in designs and mechanisms of semiconducting metal oxide nanostructures for high-precision gas sensors operated at room temperature, Materials Horizons 6 (3) (2019) 470–506.

[55] R. Ghanbari, R. Safaiee, M. H. Sheikhi, M. M. Golshan, Z. K. Horastani, Graphene decorated with silver nanoparticles as a low-temperature methane gas sensor, ACS applied materials & interfaces 11 (24) (2019) 21795–21806.

[56] G. M. Gibson, B. Sun, M. P. Edgar, D. B. Phillips, N. Hempler, G. T. Maker, G. P. A. Malcolm, M. J. Padgett, Real-time imaging of methane gas leaks using a single-pixel camera, Opt. Express 25 (4) (2017) 2998–3005. `doi:10.1364/OE.25.002998`. URL https://opg.optica.org/oe/abstract.cfm?URI=oe-25-4-2998

[57] M. Triki, T. N. Ba, A. Vicet, Compact sensor for methane detection in the mid infrared region based on quartz enhanced photoacoustic spectroscopy, Infrared Physics & Technology 69 (2015) 74–80.

[58] M. Butt, S. Degtyarev, S. Khonina, N. Kazanskiy, An evanescent field absorption gas sensor at mid-ir 3.39 μm wavelength, Journal of Modern Optics 64 (18) (2017) 1892–1897.

[59] D. Zimmerle, T. Vaughn, C. Bell, K. Bennett, P. Deshmukh, E. Thoma, Detection limits of optical gas imaging for natural gas leak detection in realistic controlled conditions, Environmental science & technology 54 (18) (2020) 11506–11514.

[60] C. Massie, G. Stewart, G. McGregor, J. R. Gilchrist, Design of a portable optical sensor for methane gas detection, Sensors and Actuators B: Chemical 113 (2) (2006) 830–836.

[61] M. Mhanna, M. Sy, A. Farooq, A selective laser-based sensor for fugitive methane emissions, Scientific reports 13 (1) (2023) 1573.

[62] L. Tyagi, R. Devi, S. Tyagi, V. Kumar, K. Sharma, Y. K. Gautam, A. Kumar, S. Kapoor, A. Bhardwaj, A. Kumar, Environmental impacts and recent advancements in the sensing of methane: a review, Environmental Technology Reviews 14 (1) (2025) 191–212.

[63] A. T. Lando, H. Nakayama, T. Shimaoka, Application of portable gas detector in point and scanning method to estimate spatial distribution of methane emission in landfill, Waste Management 59 (2017) 255–266.

[64] I. Hatipoglu, A. Nakhmani, Unsynchronized scanning with a low-cost laser range finder for real-time range imaging, in: Videometrics, Range Imaging, and Applications XIV, Vol. 10332, SPIE, 2017, pp. 78–92.

[65] J. T. Thielemann, A. Berge, Ø. Skotheim, T. Kirkhus, Fast high resolution 3d laser scanning by real-time object tracking and segmentation, in: 2012 IEEE/RSJ International Conference on Intelligent Robots and Systems, IEEE, 2012, pp. 3899–3906.

[66] L. Fu, S. You, G. Li, Z. Fan, Enhancing methane sensing with ndir technology: Current trends and future prospects, Reviews in Analytical Chemistry 42 (1) (2023) 20230062.

[67] M. Kutila, P. Pyykönen, W. Ritter, O. Sawade, B. Schäufele, Automotive lidar sensor development scenarios for harsh weather conditions, in: 2016 IEEE 19th International Conference on Intelligent Transportation Systems (ITSC), IEEE, 2016, pp. 265–270.

[68] K. A. Klise, B. L. Nicholson, C. D. Laird, Sensor placement optimization using chama, Tech. rep., Sandia National Lab.(SNL-NM), Albuquerque, NM (United States) (2017).

[69] L. Patel, J. P. Zenker, Assessing the design of integrated methane sensing networks, Environmental Research Letters 19 (12) (2024) 124011.

[70] K. A. Klise, B. L. Nicholson, C. D. Laird, A. P. Ravikumar, A. R. Brandt, Sensor placement optimization software applied to site-scale methane-emissions monitoring, Journal of Environmental Engineering 146 (7) (2020) 04020054.

[71] G. K. Sinha, Sensor data analytics for optimized methane leak detection and mitigation.

[72] Q. Chen, Y. Kimura, D. T. Allen, Defining detection limits for continuous monitoring systems for methane emissions at oil and gas facilities, Atmosphere 15 (3) (2024) 383.

[73] H. Wang, X. Fan, H. Jian, F. Yan, Exploiting the matched filter to improve the detection of methane plumes with sentinel-2 data, Remote Sensing 16 (6) (2024) 1023.

[74] M. Jia, W. Daniels, D. Hammerling, Comparison of the gaussian plume and puff atmospheric dispersion models for methane modeling on oil and gas sites (2023).

[75] S. N. Riddick, M. Mbua, R. Brouwer, E. W. Emerson, A. Anand, E. Kiplimo, S. Ojomu, J.-H. Lo, D. J. Zimmerle, Comparison of sub-ppm instrument response suggests higher detection limits could be used to quantify methane emissions from oil and gas infrastructure, Sensors 24 (11) (2024) 3407.

[76] Q. Chen, C. Schissel, Y. Kimura, G. McGaughey, E. McDonald-Buller, D. T. Allen, Assessing detection efficiencies for continuous methane emission monitoring systems at oil and gas production sites, Environmental science & technology 57 (4) (2023) 1788–1796.

[77] Maximizing Battery Life: Some of the Most Important Things to Consider When Maintaining Your AGM Battery - Fullriver Battery Blog, section: Articles (Sep. 2024). URL https://fullriverbattery.com/articles/maximizing-battery-life-some-of-the-most-important-

[78] Alicat Scientific, Gas flow controller manual, https://www.duniway.com/sites/default/files/Alicat_Gas_Flow_Controller_Manual.pdf, retrieved June 21, 2025 (n.d.).

Appendix A

Test Site Layout

The test site layout is shown in Figure A.1 and simulates a typical O&G wellhead configuration. The region outlined in blue (A) in the figure shows the CM solution deployment, while the region outlined in orange (B) shows the CRR and supporting equipment including the mast, and gas trailer, as specified in table 4.1

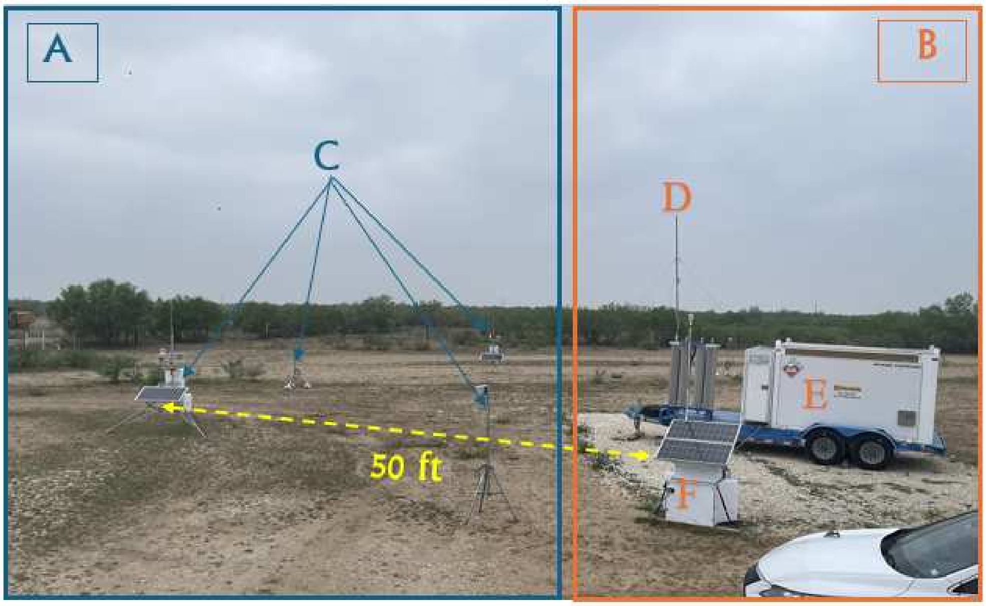

Figure A.1: Test site showing the CNG trailer, gas release mast, CRR and anemometer (with 2 solar panels) in the forefront, and several sensors (with and without solar panels).

A description of the test site layout and the solution deployment strategy are crucial to understanding single-blind test results and providing appropriate context to the performance assessment of the CM solution. The Test Center's CRR releases gas from the mast to simulate wellheads of varying heights. The CM solution uses six TDLAS based sensors (two with weather stations) to form their PSN. The sensors are spaced radially, 52 ft from the release mast, as shown in Figure A.1. A weather station attached to the CRR measures wind speed and direction, and a CNG trailer supplies the CRR with Natural Gas (NG) for the controlled releases to the atmosphere that are to be detected by the solution.

Table A.1: Figure A.1 Legend description.

Label	Description
A	CM Solution's equipment and layout
B	Test Center's CRR equipment and layout
C	Six TDLAS sensors
D	Release mast
E	Compressed natural gas trailer
F	The controlled release rig

Appendix B

Graphical User Interface of the CRR

A Graphical User Interface (GUI) was developed in this study to interact with the CRR and carry out the controlled release testing. As stated in Chapter Three, Python code was written and used to generate the test plans based on the predefined protocol and saved as a CSV file in the format SBTDatetime.csv. This CSV file would be uploaded to the web server which has a back-end code written in Python language to carry out required execution with the interaction of the GUI. Figure B.1 shows the initial state of the interface when the test plan has been uploaded as 'SBT20240426180000.csv'. In this study, to execute the single-blind controlled release testing, tests were deployed using Valve 1 and the execution of the test begins by clicking the test 'Run Test' button. Figure B.2 shows that the CNG is open, indicating the supply of gas is on, which is why we can see the blue tick shown in Figure B.2. The interface also receives and displays the output reported by the CM solution under test.

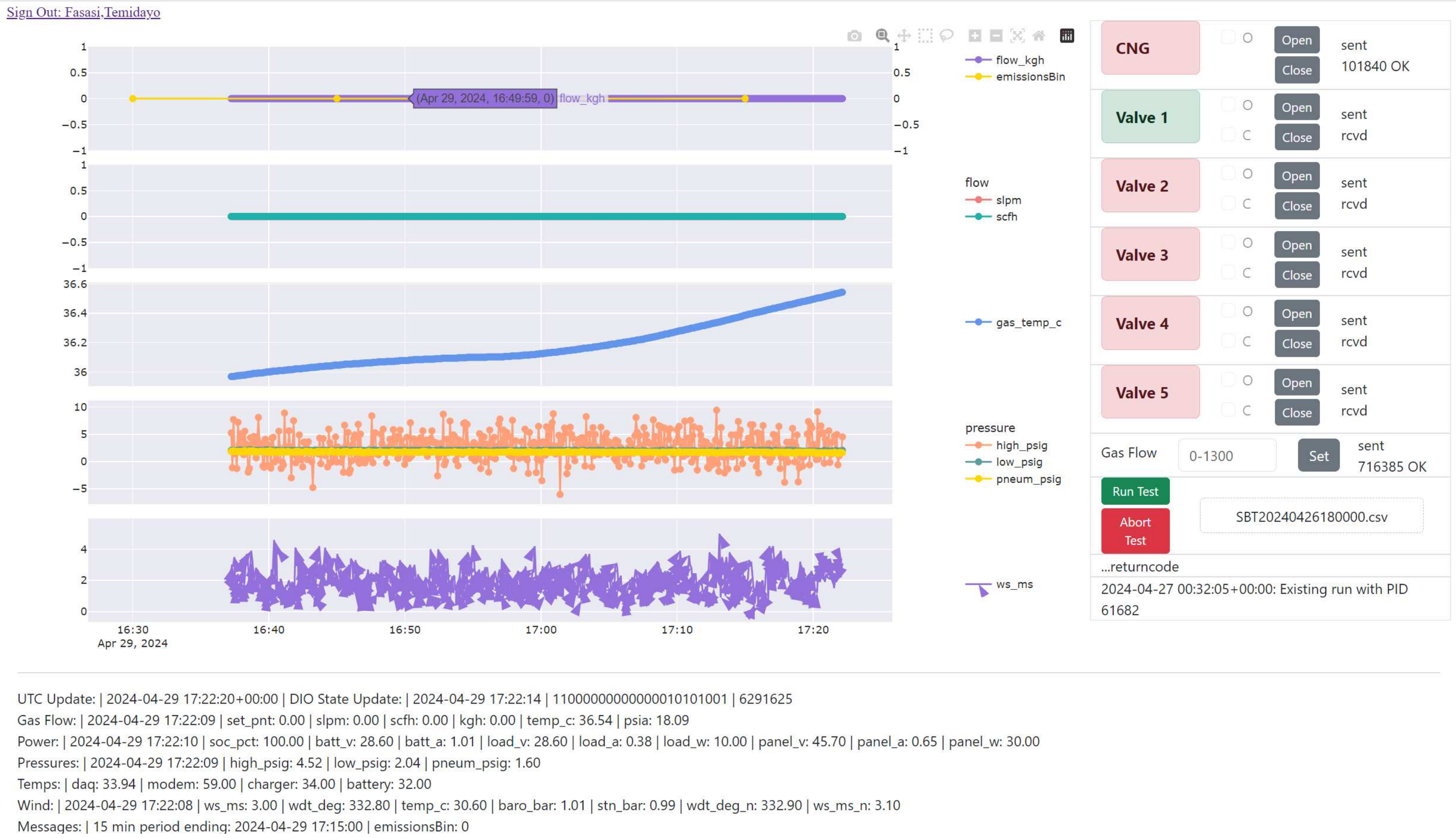

SBT20240426180000.csv

2024-04-27 00:32:05+00:00: Existing run with PID 61682

UTC Update: | 2024-04-29 17:22:20+00:00 | DIO State Update: | 2024-04-29 17:22:14 | 11000000000000010101001 | 6291625
Gas Flow: | 2024-04-29 17:22:09 | set_pnt: 0.00 | slpm: 0.00 | scfh: 0.00 | kgh: 0.00 | temp_c: 36.54 | psia: 18.09
Power: | 2024-04-29 17:22:10 | soc_pct: 100.00 | batt_v: 28.60 | batt_a: 1.01 | load_v: 28.60 | load_a: 0.38 | load_w: 10.00 | panel_v: 45.70 | panel_a: 0.65 | panel_w: 30.00
Pressures: | 2024-04-29 17:22:09 | high_psig: 4.52 | low_psig: 2.04 | pneum_psig: 1.60
Temps: | daq: 33.94 | modem: 59.00 | charger: 34.00 | battery: 32.00
Wind: | 2024-04-29 17:22:08 | ws_ms: 3.00 | wdt_deg: 332.80 | temp_c: 30.60 | baro_bar: 1.01 | stn_bar: 0.99 | wdt_deg_n: 332.90 | ws_ms_n: 3.10
Messages: | 15 min period ending: 2024-04-29 17:15:00 | emissionsBin: 0

Figure B.1: Graphical user interface at the stage of test plan upload.

Sign Out: Fasasi,Temidayo

CNG ☑ ○ sent 112697 OK

Valve 1 ○ C sent 210769 OK

Valve 2 ○ C sent rcvd

Valve 3 ○ C sent rcvd

Valve 4 ○ C sent rcvd

Valve 5 ○ C sent rcvd

Gas Flow 0-1300 sent 719876 OK

79171

SBT20240429200000.csv

Process 79171 status: sleeping

2024-04-29 19:55:49+00:00: Starting SBT20240429200000.csv

UTC Update: | 2024-04-29 20:02:03+00:00 | DIO State Update: | 2024-04-29 20:01:54 | 110010000000000010101001 | 6553769
Gas Flow: | 2024-04-29 20:01:54 | set_pnt: 351.79 | slpm: 351.76 | scfh: 745.34 | kgh: 14.03 | temp_c: 38.70 | psia: 108.68
Power: | 2024-04-29 20:01:49 | soc_pct: 100.00 | batt_v: 27.20 | batt_a: 0.91 | load_v: 27.20 | load_a: 0.77 | load_w: 20.00 | panel_v: 45.00 | panel_a: 0.57 | panel_w: 26.00
Pressures: | 2024-04-29 20:01:54 | high_psig: 192.72 | low_psig: 92.23 | pneum_psig: 50.49
Temps: | daq: 37.36 | modem: 62.00 | charger: 37.00 | battery: 36.00
Wind: | 2024-04-29 20:01:58 | ws_ms: 0.80 | wdt_deg: 258.10 | temp_c: 35.30 | baro_bar: 1.01 | stn_bar: 0.99 | wdt_deg_n: 258.60 | ws_ms_n: 0.70
Messages: | 15 min period ending: 2024-04-29 20:00:00 | emissionsBin: 0

Figure B.2: Graphical user interface while test is running, showing Valve 1 and CNG open, and the performance of the CM solution with the aid of streamplots.

Appendix C

Determination of CM Solution's Performance Metrics

Table C.1: Performance metrics for solution emissions classification using the confusion matrix.

	Solution (emissionsBin)		
	Negative (0)	Positive (1,2,3)	
Test Center	TN	FP	Rates
	FN	TP	
Negative Predictive Value (NPV)		NPV = $\frac{TN}{TN+FN}$	True Negative Rate (TNR) = $\frac{TN}{TN+FP}$
False Discovery Rate (FDR)		FDR = $\frac{FP}{TP+FP}$	False Positive Rate (FPR) = $\frac{FP}{FP+TN}$
False Omission Rate (FOR)		FOR = $\frac{FN}{FN+TN}$	False Negative Rate (FNR) = $\frac{FN}{FN+TP}$
Positive Predictive Value (PPV)		PPV = $\frac{TP}{TP+FP}$	True Positive Rate (TPR) = $\frac{TP}{TP+FN}$
Accuracy (ACC)			ACC = $\frac{(TP+TN)}{(TP+FP+TN+FN)}$

Table C.1 shows the relationship of how the performance metrics of the solution were estimated using the confusion matrix value shown in Figure 4.2. The confusion matrix shows that :

- True Negatives (TN) = 4736
- False Positives (FP) = 9
- False Negatives (FN) = 59
- True Positives (TP) = 349

Now, using the given equations: True Negative Rate (TNR)

$$\mathrm{TNR} = \frac{\mathrm{TN}}{\mathrm{TN} + \mathrm{FP}} = \frac{4736}{4736 + 9} = 0.998 \tag{C.1}$$

False Positive Rate (FPR)

$$\mathrm{FPR} = \frac{\mathrm{FP}}{\mathrm{FP} + \mathrm{TN}} = \frac{9}{9 + 4736} = 0.002 \tag{C.2}$$

False Negative Rate (FNR)

$$\mathrm{FNR} = \frac{\mathrm{FN}}{\mathrm{FN} + \mathrm{TP}} = \frac{59}{59 + 349} = 0.145 \tag{C.3}$$

True Positive Rate (TPR)

$$\mathrm{TPR} = \frac{\mathrm{TP}}{\mathrm{TP} + \mathrm{FN}} = \frac{349}{349 + 59} = 0.855 \tag{C.4}$$

Negative Predictive Value (NPV)

$$\mathrm{NPV} = \frac{\mathrm{TN}}{\mathrm{TN} + \mathrm{FN}} = \frac{4736}{4736 + 59} = 0.988 \tag{C.5}$$

False Discovery Rate (FDR)

$$\mathrm{FDR} = \frac{\mathrm{FP}}{\mathrm{FP} + \mathrm{TP}} = \frac{9}{9 + 349} = 0.025 \tag{C.6}$$

False Omission Rate (FOR)

$$\text{FOR} = \frac{\text{FN}}{\text{FN} + \text{TN}} = \frac{59}{59 + 4736} = 0.012 \tag{C.7}$$

Positive Predictive Value (PPV)

$$\text{PPV} = \frac{\text{TP}}{\text{TP} + \text{FP}} = \frac{349}{349 + 9} = 0.975 \tag{C.8}$$

Accuracy (ACC)

$$\text{ACC} = \frac{\text{TP} + \text{TN}}{\text{TP} + \text{FP} + \text{TN} + \text{FN}} = \frac{349 + 4736}{349 + 9 + 4736 + 59} = 0.987 \tag{C.9}$$

Appendix D

On-site vs Local Winds: The CRR Anemometer

Winds were predominantly from the southeast during the SBT period, as shown in Figure D.1. Each of these figures spans the SBT period (March 12- May 8, 2024).

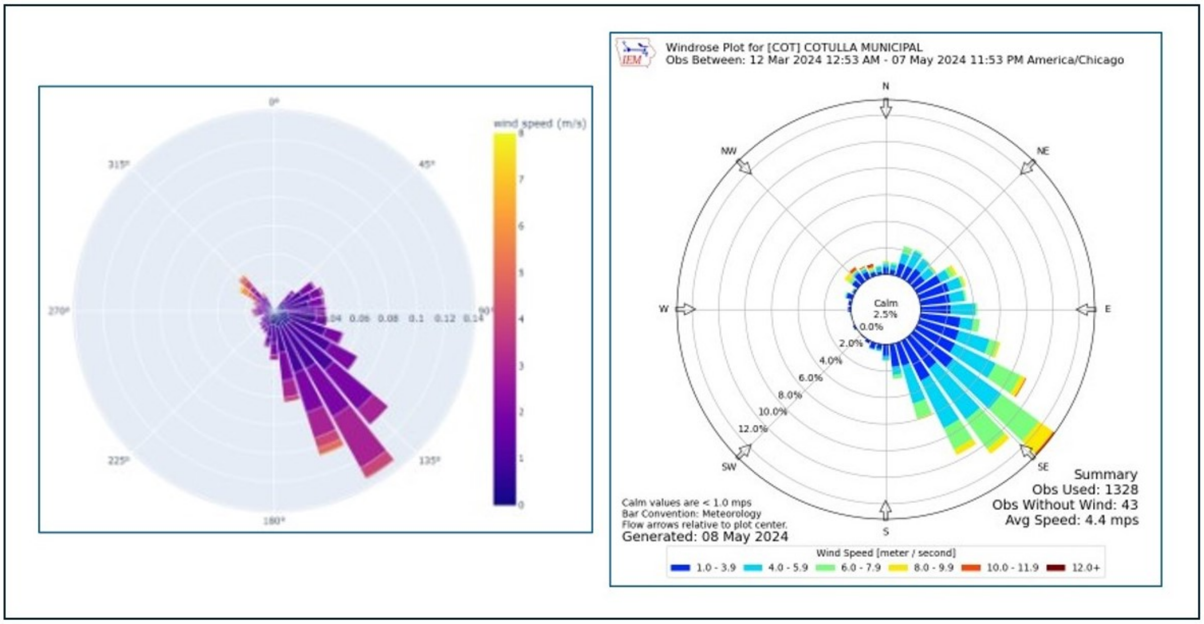

Figure D.1: Wind roses covering the majority of the SBT period. The left panel was recorded by the anemometer on the CRR, the right panel is from a nearby municipal airport. They show good qualitative agreement.

Appendix E

Electrical Wiring Configuration of the CRR

The wiring for the CRR is shown in Figure E.1. The actuation valves (AV 1 to AV 5) in Table E.1 through Table E.2 denote the Actuation Valve (AV) 1 through AV 5 respectively. The tables outline the wiring connections and how the coils and limit switches are wired to the COMMS for interaction and execution of the control system algorithms. For example, the positive close coil of the AV 1 is registered on the Modbus 2008 and connected to the EIOO terminal on the external board PS12DC attached to the T7 lab jack through DB15 pin as illustrated in Figure E.1. Consequently, Figure E.1 shows the wiring of the limit switches, detailing cable color code further illustrated in the process and instrumentation diagram shown in Figure E.2.

Table E.1: Table 1/2 of part connections and electrical wiring.

Part	Connection	Valve Color	Cable Color	LJ Pin	ExBoard	Exboard Pin	LJ MB Reg
AV1	close_coil+	-	-	EIO0	PS12DC	S0	2008
AV1	close_coil-	-	-	Gnd	Gnd	Gnd	
AV1	open_coil+	-	-	EIO1	PS12DC	S1	2009
AV1	open_coil-	-	-	Gnd	Gnd	Gnd	
AV1	close_lim_nc_1	red	red	Vs	Vs	Vs	
AV1	close_lim_c_2	blk	blk	FIO0	DB37	FIO0	2000
AV1	close_lim_no_3	blue	green	Gnd	Gnd	Gnd	
AV1	open_lim_nc_4	yellow	yellow	Vs	Vs	Vs	
AV1	open_lim_c_5	white	orange	FIO1	DB37	FIO1	2001
AV1	open_lim_no_6	brown	brown	Gnd	Gnd	Gnd	

Table E.2: Table 2/2 of part connections and electrical wiring.

Part	Connection	Valve Color	Cable Color	LJ Pin	ExBoard	Exboard Pin	LJ MB Reg
AV2	close_coil+	-	-	EIO2	PS12DC	S2	2010
AV2	close_coil-	-	-	Gnd	Gnd	Gnd	
AV2	open_coil+	-	-	EIO3	PS12DC	S3	2011
AV2	open_coil-	-	-	Gnd	Gnd	Gnd	
AV2	close_lim_nc_1	red	red	Vs	Vs	Vs	
AV2	close_lim_c_2	blk	blk	FIO2	DB37	FIO2	2002
AV2	close_lim_no_3	blue	green	Gnd	Gnd	Gnd	
AV2	open_lim_nc_4	yellow	yellow	Vs	Vs	Vs	
AV2	open_lim_c_5	white	orange	FIO3	DB37	FIO3	2003
AV2	open_lim_no_6	brown	brown	Gnd	Gnd	Gnd	
AV3	close_coil+	-	-	EIO4	PS12DC	S4	2012
AV3	close_coil-	-	-	Gnd	Gnd	Gnd	
AV3	open_coil+	-	-	EIO5	PS12DC	S5	2013
AV3	open_coil-	-	-	Gnd	Gnd	Gnd	
AV3	close_lim_nc_1	red	red	Vs	Vs	Vs	
AV3	close_lim_c_2	blk	blk	FIO4	DB37	FIO4	2004
AV3	close_lim_no_3	blue	green	Gnd	Gnd	Gnd	
AV3	open_lim_nc_4	yellow	yellow	Vs	Vs	Vs	
AV3	open_lim_c_5	white	orange	FIO5	DB37	FIO5	2005
AV3	open_lim_no_6	brown	brown	Gnd	Gnd	Gnd	
AV4	close_coil+	-	-	EIO6	PS12DC	S6	2014
AV4	close_coil-	-	-	Gnd	Gnd	Gnd	
AV4	open_coil+	-	-	EIO7	PS12DC	S7	2015
AV4	open_coil-	-	-	Gnd	Gnd	Gnd	
AV4	close_lim_nc_1	red	red	Vs	Vs	Vs	
AV4	close_lim_c_2	blk	blk	FIO6	DB37	FIO6	2006
AV4	close_lim_no_3	blue	green	Gnd	Gnd	Gnd	
AV4	open_lim_nc_4	yellow	yellow	Vs	Vs	Vs	
AV4	open_lim_c_5	white	orange	FIO7	DB37	FIO7	2007
AV4	open_lim_no_6	brown	brown	Gnd	Gnd	Gnd	
AV5	close_coil+	-	-	CIO0	PS12DC	S8	2016
AV5	close_coil-	-	-	Gnd	Gnd	Gnd	
AV5	open_coil+	-	-	CIO1	PS12DC	S9	2017
AV5	open_coil-	-	-	Gnd	Gnd	Gnd	
AV5	close_lim_nc_1	red	red	Vs	Vs	Vs	
AV5	close_lim_c_2	blk	blk	MIO0	DB37	MIO0	2020
AV5	close_lim_no_3	blue	green	Gnd	Gnd	Gnd	
AV5	open_lim_nc_4	yellow	yellow	Vs	Vs	Vs	
AV5	open_lim_c_5	white	orange	MIO1	DB37	MIO1	2021
AV5	open_lim_no_6	brown	brown	Gnd	Gnd	Gnd	

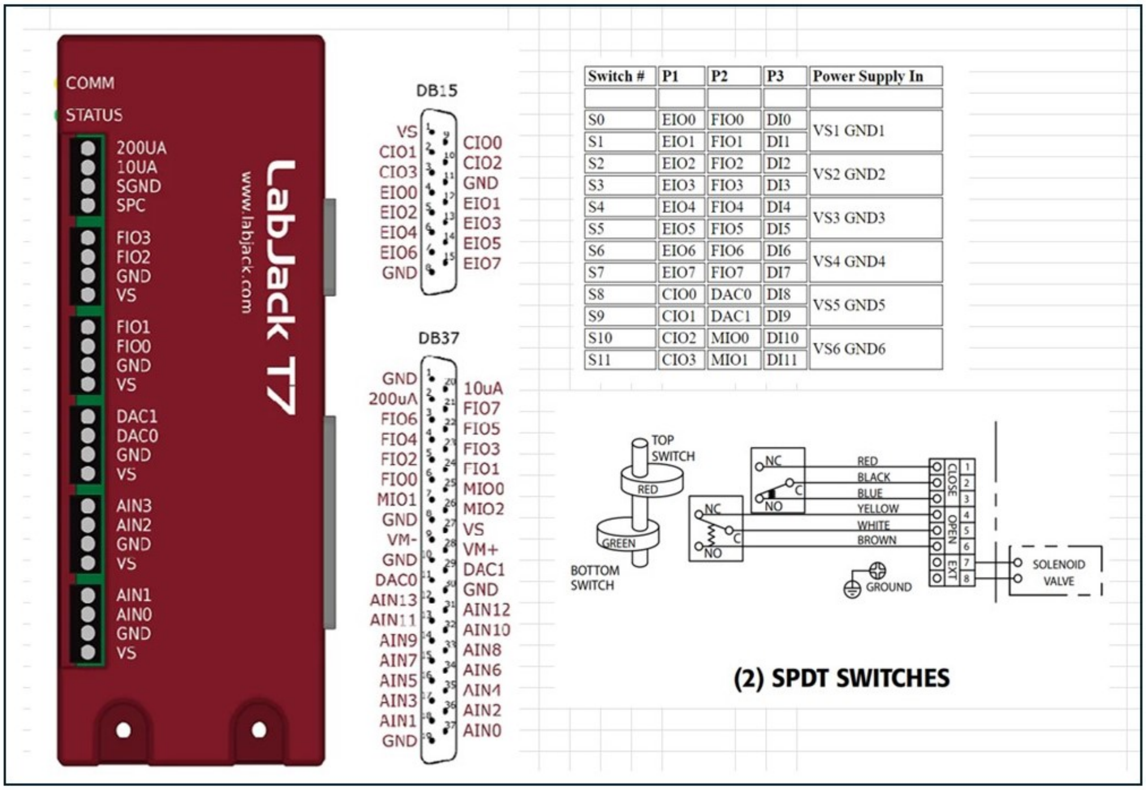

Switch #	P1	P2	P3	Power Supply In
S0	EIO0	FIO0	DI0	VS1 GND1
S1	EIO1	FIO1	DI1	
S2	EIO2	FIO2	DI2	VS2 GND2
S3	EIO3	FIO3	DI3	
S4	EIO4	FIO4	DI4	VS3 GND3
S5	EIO5	FIO5	DI5	
S6	EIO6	FIO6	DI6	VS4 GND4
S7	EIO7	FIO7	DI7	
S8	CIO0	DAC0	DI8	VS5 GND5
S9	CIO1	DAC1	DI9	
S10	CIO2	MIO0	DI10	VS6 GND6
S11	CIO3	MIO1	DI11	

Figure E.1: Communication system wiring configuration and limit switch actuation for normally closed, common, and normally open contact points with respect to its designated color code.

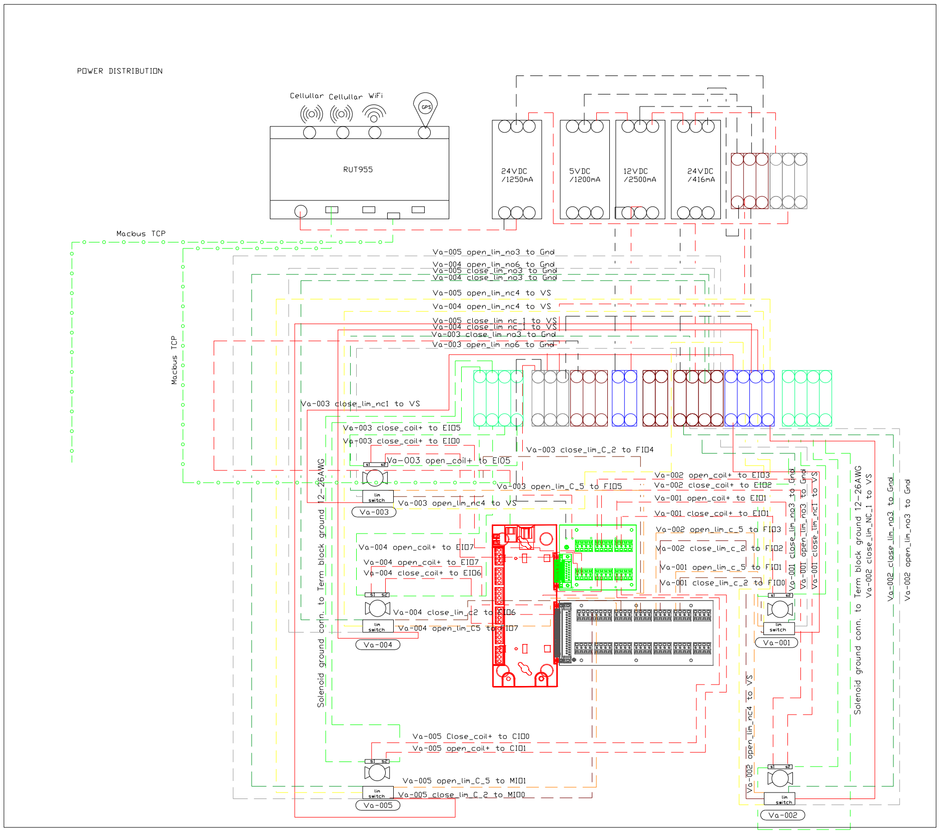

Figure E.2: Process and instrumentation diagram: Electrical.

Appendix F

Bill of Materials

Table F.1: Bill of materials.

Description	SubAssy	Vendor	Vendor Part Number	Mfr Part Number	BOM Qty
High Flow Meter	Alicats	Alicat	-	MCR-2000SLPM	1
Medium Flow Meter	Alicats	Alicat	-	MCP-250SLPM	1
Low Flow Meter	Alicats	Alicat	-	MC-50SLPM	1
SS Swagelok Tube Fitting, M CONN, 3/8 in.	Alicats	Swagelok	SS-600-1-4	-	6
Nickel Plated Brass M20 x 1.5 Standard Fitting	Alicats	SealCon	CD20MA-MX	1.610.2000.50	2
316 SS Threaded LP Bushing Adapter, 3/4 M x	Alicats	McMaster	4452K168	-	1
CABLE CAT6 8COND 23AWG BLK 50′	Alicats	Digikey	C7136100B-50-ND	7136100	2
Pull through RJ45 plug CAT6 UNSH	Alicats	Digikey	5073-TDPTC6-ND	TDPTC6	2
RJ45, Ethernet 1.00" (304.8mm) Unshielded	Alicats	Digikey	TL1463-ND	N200-001-BK	2
5.5x2.1mm round right angle barrel jack	Alicats	Digikey	839-1626-ND	10-02224	2
18 AWG Stranded TFFN green	Alicats	DWC	-	-	2
Vinyl Insulated Ring Terminals	Alicats	McMaster	7113k612	-	5
CABLE 3COND 16AWG BLACK 100′	Alicats	Digikey	A1953/3TB-100-ND	1953/3T BKO03	3
CONN TERM BLK GROUND 12-26AWG	Alicats	Digikey	277-2031-ND	3044092	2
CONN TERM BLK FEED THRU 12-26AWG	Alicats	Digikey	277-2026-ND	3044076	2
CONN TERM BLK GROUND 12-26AWG	Alicats	Digikey	277-3329-ND	3045088	2
CONN TERM BLK END PLATE RAIL GRY	Alicats	Digikey	277-2038-ND	3047028	2
JUMPER TERM BLK 2POS FLAT PIN	Alicats	Digikey	277-2115-ND	3030161	2
Nickel Plated Brass M20 x 1.5 Standard Fitting	Alicats	SealCon	CD20MA-MX	1.610.2000.50	1
20.00x16.00x10.00, Hoffman	Boxes	Digikey	CSD201610	-	1
Hoffman white panel for 2016	Boxes	Digikey	1441-1408-ND	CP2016	1
16.00x12.00x8.00, Hoffman	Boxes	Digikey	CSD16128	-	1
Hoffman white panel for 1612	Boxes	Digikey	1441-1405-ND	CP1612	1
Hoffman Locking handle	Boxes	Digikey	1441-1458-ND	CWHK	1
HP Filter Unknown Ports, 3600 psig max press	Flow	Ame CNG	F112-G6-K1	-	1
AMERICAN CNG COALESCING FILTER ELEMENT	Flow	Ame CNG	A-F112-66-OL	-	1
ROTAREX EVO SIRIUS REGULATOR	Flow	Ame CNG	RO-EVO-110S	-	1
SOLENOID WIRE CONNECTOR	Flow	Ame CNG	A-RSC120-A1	-	1
25′ Flex Hose Assembly 3/8" Compression x	Flow	Ame CNG	custom built to order	-	1
Pressure transducer	Flow	Amazon	RO-EVO-110S	-	1
Triple-Lok® 37° Flare JIC Fittings and Adapter	Flow	MFCP	-	6 HX6-S	2
37° Flare Connector M- JIC to 3/8 tube compression	Flow	MFCP	-	6-6 XHBZ-SS	2
SAE-6 ORB9/16-18 to 3/8 Tube	Flow	MFCP	-	6-6 ZHBA-SS	2
1/4" MBSPP-ORR x 1/4" FNPT Steel Adapter	Flow	MFCP	-	1/4X1/4F40HGS	2
SS Swagelok Tube Fitting, M CONN, 3/8 in.	Flow	Swagelok	SS-600-1-4	-	6
SS Swagelok Tube Fitting, M CONN, 1/4 in.	Flow	Swagelok	SS-400-1-4	-	2
SS Swagelok Tube Union Tee, 1/4 in.	Flow	Swagelok	SS-400-3	-	1
Stainless SS Tube Fitt, Union Tee, 3/8 in. Tube OD	Flow	Swagelok	SS-600-3	-	6
Stainless SS Tube Fitt,, F Branch Tee, 3/8 in. Tube OD x 3/8 in.	Flow	Swagelok	SS-600-3TTF	-	1
Stainless SS Tube Fitt, F Connector, 3/8 in. Tube OD x 1/4 in.	Flow	Swagelok	SS-600-7-4	-	1
Stainless SS Tube Fitt,F Connector, 1/4 in. Tube OD x 1/4 in.	Flow	Swagelok	SS-400-7-4	-	1
Stainless SS Tube Fitt, Reducing Union, 1/2 in. x 3/8 in.	Flow	Swagelok	SS-810-6-6	-	5
M20 x 1.5 Nickel Plated Brass (2 Hole) Gland	Flow	SealCon	CD20M4-MX	1.687.2003.50	1

Table F.2: Bill of materials - additional items.

Description	SubAssy	Vendor	Vendor Part Number	Mfr Part Number	BOM Qty
M20 x 1.5 Nickel Plated Brass (3 Hole) Gland	Flow	SealCon	CD20M5-BR	1697200450	1
1-1/4 x 2 in. Steel 2-Hole 90-Degree Angle Fitting, Pack of 50	Frame	Winlectric	AB202 EG	61601301094	14
1-5/8 in. Electro Galvanized Steel 2-Hole 90-Degree Angle Fitt.	Frame	Winlectric	AB201 EG	61601325714	4
1/2-13 channel nuts	Frame	Winlectric	17442	60198617442	38
1/2-13 channel bolts	Frame	nan	-	-	38
3/8-16 channel nuts	Frame	Winlectric	17420	60198617420	16
3/8-16 channel bolts	Frame	nan	30980	60198630980	16
1/4-20 channel nuts	Frame	Winlectric	17430	60198617430	3
Deep strut 10 ft	Frame	Winlectric	-	-	3
Shallow strut 10 ft	Frame	Winlectric	-	-	2
Strut Hinges	Frame	McMaster	3505T12	-	2
1x1x.125 angle x 3ft	Frame	McMaster	8968K12	-	-
odyssey extreme agm	Power	battery mart	-	PC1200MJ	2
Nickel Plated Brass M20 x 1.5 Standard Fitt.	Power	SealCon	CD20MA-MX	1.610.2000.50	2
T7 Labjack	SCADA	Labjack	T7	T7	1
PS12DC Power Switching Board	SCADA	Labjack	relay board	PS12DC	1
CB37 Terminal Board	SCADA	Labjack	expansion card	CB37	1
airmar 200/cable/RH sensor	SCADA	iMarine	WS-200WX-RS232-RH	WS-200WX-RS232-IPX6	1
RUT956 modem, all carriers US	SCADA	Digikey	4703-RUT956A00A00-ND	-	1
Limit switch	Valves	Latech/AT-Controls	-	22-TX-025/3RDD-XB	5
2" IMC conduit nipples	Valves	Winlectric	-	64325	10
1/2 rigid water-tight conduit hub	Valves	Winlectric	-	91631	10
LP Galvanized Steel Fitt.	Valves	McMaster	1162T42	-	5
Ex-e 3/4 NPT Nickel Plated Brass	Valves	SealCon	CD21NP-MX	1.687.3499.70	5
Nickel Plated Brass M20 x 1.5	Valves	SealCon	CD20MR-MX	1.610.2000.51	5
SENSOR SEALED GAUGE 0-200 PSI	Flow	Digikey	480-5152-ND	MLH200PSL01A	2
Fast acting pressure relief valve	Flow	McMaster	5784T12	-	1
GH10 - 316 Stainless Steel Regulator	Flow	ITT Conoflow	GH10XTHMAXXG	-	1
Power supply out 24VDC/1250mA	SCADA	Digikey	102-6034-ND	PYBE30-Q24-S24-DIN	1
Power supply out 12VDC/2500mA	SCADA	Digikey	102-6032-ND	PYBE30-Q24-S12-DIN	1
Power supply out 5VDC/1200mA	SCADA	Digikey	102-4579-ND	PQDE6W-Q24-S5-DIN	1
Power supply out 24VDC/416mA	SCADA	Digikey	102-3125-ND	PYB10-Q24-S24-DIN	1
JUMPER TERM BLK 2POS FLAT PIN	SCADA	Digikey	277-2115-ND	3030161	10
CONN BACKSHELL 9POS 180DEG SHLD	SCADA	Digikey	909GME-ND	977-009-020R121	1
CONN D-SUB PLUG 9POS SLDR CUP	SCADA	Digikey	609-1524-ND	DE09P064TXLF	2
CONN TERM BLK DISCONN 10-26AWG	SCADA	Digikey	277-2034-ND	3046032	5
FUSE MODULAR TERMINAL BLOCK CONN	SCADA	Digikey	3212172	3212172	1
14" DIN RAIL (35x7.5mm)	SCADA	Digikey	ADR3575-S1400-ND	TS3575SL	3
FUSE GLASS 100MA 250VAC 5X20MM	SCADA	Digikey	F1715-ND	0217.100MXP	5
CBL USB2.0 A PLUG TO B PLUG 3’	SCADA	Digikey	380-1424-ND	SC-2ABE003F	1
CABLE USB RS232 5V WIRE END 1.8M	SCADA	Digikey	768-1078-ND	USB-RS232-WE-1800-BT$_5$.0	1

Appendix G

Process and Instrumentation Diagram: Mechanical

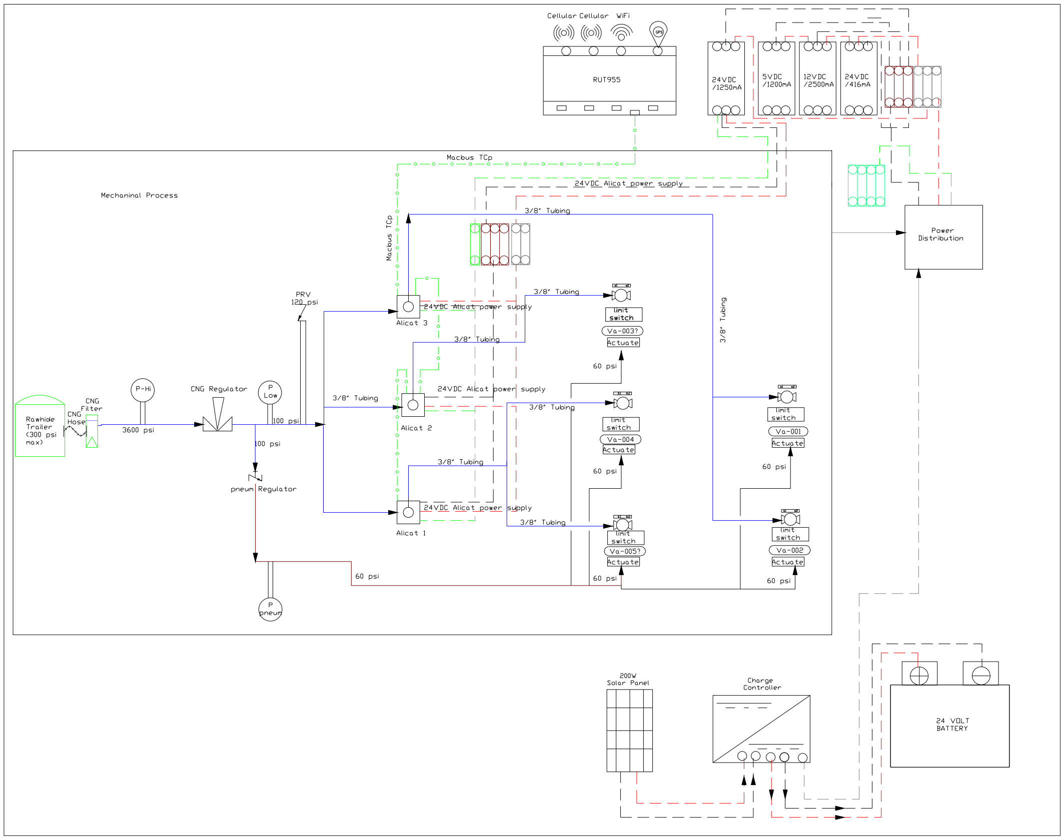

Figure G.1: Process and instrumentation diagram: Mechanical.

List of Abbreviations

ADED	Advanced Development of Emissions Detection
AGM	Absorbent Glass Mat
ARPA-E	Advanced Research Projects Agency-Energy
AV	Actuation Valve
$\mathbf{CH_4}$	Methane
CFR	Code of Federal Regulations
CM	Continuous Monitoring
CNG	Compressed Natural Gas
COMMS	Communication System
CSV	Comma-Separated Values
$\mathbf{CO_2}$	Carbon-dioxide
CRR	Controlled Release Rig
CSU	Colorado State University
CSV	Comma Separated Value
DIAL	Differential Absorption LiDAR
DFB-QCL	Distributed Feedback Quantum Cascade Lasers
DFB-ICL	Interband Cascade Laser
DFB-LD	Distributed Feedback Laser Diode
EPA	U.S. Environmental Protection Agency
FDR	False Discovery Rate
FNR	False Negative Rate
FNF	False Negative Fraction
FPF	False Positive Fraction
FP	False Positive
FPR	False Positive Rate

GHG	Greenhouse Gas
GUI	Graphical User Interface
GWP	Global Warming Potential
IR	Infrared Radiation
IPCC	Intergovernmental Panel on Climate Change
OGMP	Oil & Gas Methane Partnership
LDAR	Leak Detection and Repair
MDL	Minimum Detection Limit
MET	Meteorological
METEC	Methane Emission Technology Evaluation Center
MONITOR	Methane Observation Networks with Innovative Technology to Obtain Reductions
MQTT	Message Queuing Telemetry Transport
MPPT	Maximum Power Point Tracking
NDIR	Non-Dispersive Infrared
NG	Natural Gas
O&G	Oil and Gas
OGI	Optical Gas Imaging
POR	Probability of Reporting
PSN	Point Sensor Network
PPV	Positive Predictive Value
REDOX	oxidation-reduction
SMO	Semiconducting Metal Oxide
TDLAS	Tunable Diode Laser Absorption Spectroscopy
TNR	True Negative Rate
TPR	True Positive Rate
U.S.	United States